# Rubidium spectroscopy inside hollow core fibers

written by

**Maik Selch**

Bachelor thesis in physics
submitted to the Fachbereich Physik, Mathematik und Informatik (FB 08)
of the Johannes Gutenberg-Universität Mainz
on 28.11.2016

first examiner: Prof. Dr. Patrick Windpassinger
second examiner: Prof. Dr. Klaus Wendt

Hereby, I ensure that I have written this thesis myself without using any other sources than given and marked quotes properly.

Mainz, the [Datum] [Unterschrift]

Maik Selch
Quantum
Institut für Physik
Staudingerweg 7
Johannes Gutenberg-Universität D-55099 Mainz
mselch@students.uni-mainz.de

# Contents

# 1. Motivation

The atomic and molecular discrete transition line systems are a fascinating quantum feature within the bounds of electromagnetical interaction. Its experimental analysis with an ever ongoing growth in precision as well as the development of manipulation techniques together with its theoretical unfolding in quantum theory led to the vast variety of applications that is taken profit of today.
The discrete atomic/molecular transition line systems are exploited in atomic clocks [1,2], atomic microwaves [3,4,5], laser frequency stabilization [6,7], laser cooling experiments [8,9,10] or the study of novel quantum phenomena [11,12].
Although these quantum systems seem to be understood very well and the underlying techniques for setting them up are (close to be) fully developed, they come out to be extremely cumbersome. While research in laboratories goes on, there is the desire to establish these outstanding laboratory performances in different branches of industry or make them available for personal usage by miniaturising the associated setup and enclosing it in an appropriate housing structure in order to finally form a stable and compact device [13,14,15,16,17,18].
Such a miniaturisation, however, incorporates its own difficulties [19]. A smaller host structure for atomic/molecular vapours reduces the signal to noise ratio by reducing the interaction length with the vapour. Moreover, as the gas host gets ever smaller, the interaction with the surrounding walls becomes ever more important. An increased interaction level with the walls of the container results in both a broadening and shifting of atomic and molecular spectral transition lines as well as dephasing effects due to physisorption and chemisorption effects on the wall's surface.
Methods developed for reducing the host structure are for example given by micro-electronic-mechanical systems or dielectric waveguide technologies [19]. The latter include hollow core photonic crystal fibers as a system of choice. The benefits of using such dielectric waveguiding geometries as hollow core photonic crystal fibers for hosting gas phase atomic and/or molecular media are offered by a very long interaction length which is possible due to low loss propagation in the waveguide, tight transverse mode confinement and easy integration with existing fiber optic systems. The optimisation of the fiber properties in this regard push the manufacturers of such fibers to fabricate many different transversal geometries as well as to integrate special inner wall coatings.
Another matter of interest for working with hollow core photonic crystal fibers is to further improve the understanding of light-matter and light-light interaction. Such fibers are usually extemely long compared to their very small transversal extents. The strong light focussing required to guide light into a fiber and the strong light confinement inside these fibers enhance the probability for light-matter/light-light

interactions to occur remarkably. For this kind of analysis, the long interaction lengths of these fibers combined with the strong light confinement provide ideal conditions.
As a result, hollow core photonic crystal fibers provide not only a promising option of choice for a miniature host structure of atomic/molecular vapours that shall give access to extraordinary spectral line manipulation performances even outside the laboratory. They are furthermore regarded as an excellent system for investigations in light-matter and light-light interaction.
This work forms part of the project "strong interactions inside hollow core fibers" in the research field of "experimental quantum optics and quantum information" in the Quantum department of the university Mainz. In this project, $^{87}$Rb atoms are cooled down by a three dimensional magneto-optical trap and guided into and inside a Kagome type hollow core photonic crystal fiber by an optical conveyor belt. The project studies photon-photon interactions in such a tight transversal fiber geometry. Once the atoms are located inside, a coherent two photon EIT process is employed to get strong effective photon-photon interactions. Additionally, strong long range atom-atom interactions are induced by exciting the rubidium atoms into highly excited states, the so called Rydberg states which provide an enormous polarizability. This enhances dipole-dipole interactions between the rubidium atoms.
In order to support the investigations, there needs to be found a hollow core fiber that optimizes the conditions for strong photon-photon interactions to occur. Therefore, a vacuum system has been set up which incorporates several of these fibers whose properties in light guiding as well as their properties in hosting rubidium atoms need to be analysed.

In this Bachelor thesis, a focus is put on investigations of the vacuum system itself, the laser beam properties in the paraxial approximation and its guidance through fibers. Three different aspects are investigated. Firstly, the light propagation of the Gaussian mode and its guidance through different fibers is analysed. Secondly, the diffusion process for rubidium atoms propagating through the chamber and into the fibers is tried to be understood by modeling it theoretically and observing it experimentally. Thirdly, the steady state rubidium pressures inside a pyrex glass cell, the vacuum chamber and five of the fibers are tried to be determined.
Within the bounds of the experiments carried out in this work, a laser diode is used that emits light at a wavelength of $780nm$ which gives access to the $^{85}Rb$ and $^{87}Rb$ $D_2$-transition line system. The used diode laser's beam propagation in free space after passing through a glass fiber cable is analysed and the optics for guiding light through the hollow core fibers distinguishing in size, cladding structure and coating is chosen and set up in the first place. Before the coupling into these fibers is done, light guidance and light propagation are investigated for a test hollow core fiber. The main set of fibers to be examined is introduced in detail. These fibers are placed inside a vacuum system where a rubidium reservoir is inserted to yield a steady rubidium influx. The rubidium atoms make their way through the vacuum system to finally diffuse into the hollow core fibers where it is crucial to know, how

the rubidium atom density inside the fibers evolves over time until reaching steady state conditions. Therefore, on the one hand, the diffusion process is calculated theoretically, making use of the diffusion equation to get an estimation of the time period the diffusion process needs to complete. On the other hand, the progress of rubidium atoms propagating through the vacuum system and entering the fibers is observed experimentally. Therefore, the transmission profile of the rubidium $D_2$-transition line system is recorded for the laser light guided through the vacuum system interacting with the rubidium. This shall allow for a comparison with the previously calculated diffusion dynamics do be done. Moreover, a model for the light-matter interaction of rubidium is presented which allows for the understanding of the experimentally observed rubidium absorption signals for the $D_2$-lines at very low intensities. The very low intensity range can be accessed experimentally inside two different rubidium gas host structures available: a pyrex glass cell and the vacuum chamber. The absorption behaviour of rubidium makes it possible to determine the particle pressures inside these host structures. In addition, also the absorption behaviour for higher intensities is analysed for both of the gas hosts. Ultimately, this thesis culminates in determining the steady state particle pressures inside several of the available hollow core fibers by extrapolating the rubidium absorption behaviour to the zero intensity limit. Furthermore, the coupling efficiencies for guiding the laser light into these fibers are presented.

In dieser Bachelorarbeit wird der Fokus auf Untersuchungen des vorliegenden Vakuumsystems, der Laserstrahleigenschaften in der Paraxialnäherung und der Lichtleitung durch Hohlkernfasern gelegt. In dieser Hinsicht werden drei Aspekte näher verfolgt. Zuerst wird die Lichtausbreitung der Gaußmode und ihre Leitung durch verschiedene Fasern analysiert. Danach wird der Diffusionsprozess von Rubidium Atomen im Vakuumsystem und insbesondere deren Diffusion in die Fasern hinein sowohl theoretisch als auch experimentell näher betrachtet. Schließlich wird der stationäre Druck der Rubidium Atome in einer Pyrexglaszelle, der vakuumkammer und in fünf der Fasern bestimmt.
Im Rahmen der Experimente, die in dieser Arbeit durchgeführt werden, wird eine Laserdiode mit einer Wellenlänge von $780nm$ benutzt, um die $D_2$-Übergänge der Isotope $^{85}$Rb und $^{87}$Rb anzuregen. Die Ausbreitung von Laserstrahlung wird im freien Raum nach Durchlaufen eines Glasfaserkabels analysiert und die Optik ausgewählt und aufgebaut, um das Laserlicht schließlich durch die verschiedenen Hohlkernfasern zu leiten, die sich in Größe, Kagome-Verkleidung und im Belag der inneren Wand unterscheiden. Bevor das Laserlicht in die Fasern eingekoppelt wird, werden Lichtausbreitung und -leitung an einer Testfaser untersucht. Die anderen Fasern, die in das Vakuumsystem integriert worden sind, werden zunächst im Detail vorgestellt. Ein Rubidium Reservoir im Inneren des Vakuumsystems garantiert einen stetigen Zufluss von Rubidium. Die Rubidium Atome diffundieren durch das Vakuumsystem, um schließlich die Fasern zu füllen. Hierbei ist es wichtig, zu wissen, wie sich die Teilchendichte von Rubidium im Laufe der Zeit entwickelt, bis ein stationärer Zustand erreicht

wird. Deshalb wird der Diffusionsprozess einerseits theoretisch behandelt, indem von der Diffusionsgleichung Gebrauch gemacht wird, und andererseits wird die Diffusion experimentell erfasst. Dazu wird das Transmissionsprofil der Rubidium $D_2$-Übergänge aufgenommen für das Laserlicht, welches durch das Vakuumsystem geleitet wird und dabei mit dem Rubidium interagiert. Dadurch können anschließend Theorie und Experiment verglichen werden. Des Weiteren wird ein Modell für die Licht-Materie Wechselwirkung für Rubidium vorgestellt, welches erlaubt, die aufgenommenen Absorptionssignale für kleine Lichtintensitäten für die $D_2$-Übergänge zu verstehen. Der Bereich kleiner Lichtintensitäten kann experimentell für zwei verfügbare, mit Rubidium gefüllte Systeme erreicht werden: einer Glaszelle aus Pyrex und der Vakuumkammer. Aus dem Absorptionsverhalten von Rubidium kann dessen Druck in diesen Systemen bestimmt werden. Zusätzlich wird auch das Absorptionsverhalten für höhere Strahlintensitäten für diese Systeme untersucht. Schließlich mündet diese Arbeit in der Bestimmung des stationären Drucks, den Rubidium in mehreren Hohlkernfasern annimmt, indem das Absorptionsverhalten zu kleinen Strahlintensitäten hin extrapoliert wird. Zudem werden die erreichten Kopplungseffizienzen für die Lichtleitung durch diese Fasern vorgestellt.

# 2. Experimental setup

The experimental setup is first to be presented, since it is on the one hand not very complex and on the other hand it is used for any experiments carried out within this thesis. "Individual" setups only vary from the presented structure by replacing, adding or removing single elements.
The setup is intended for analysing the light-matter interaction in the rubidium $D_2$-line system. A laser beam exiting a laser source is splitted into three beams whose intensity can be regulated independently. The beams shall pass three different rubidium gas host structures: a pyrex glass cell, a vacuum chamber and different types of hollow core fibers. The absorption signal is finally measured with photodiodes and displayed on an oscilloscope.

The whole setup consists of two separate blocks which are shown in the figures 2.1 and 2.2, respectively.

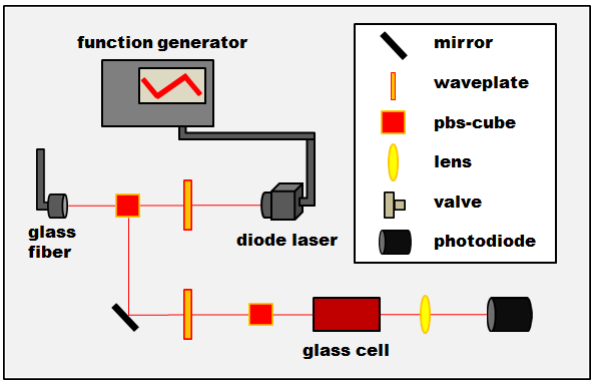


Figure 2.1.: First block of the experimental setup. A frequency/function generator outputs a triangular voltage signal that is connected to the laser diode in order to linearly sweep the frequency across the rubidium $D_2$-lines. The laser beam emitted by the laser diode is split in two to make its way into a glass fiber cable and through a rubidium filled pyrex glass cell where the absorption signal is finally detected by a photodiode.

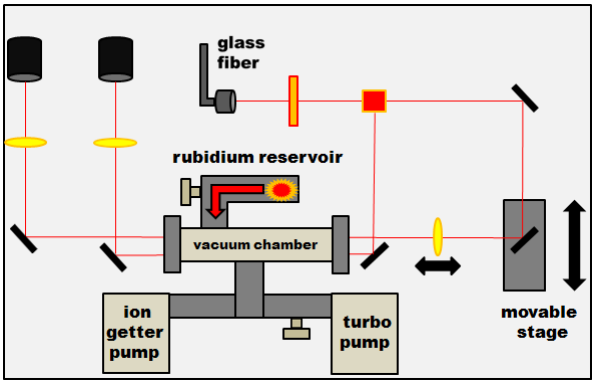


Figure 2.2.: Second block of the experimental setup. A cylindrical chamber filled with hollow core photonic crystal fibers is evacuated by a turbo and an ion getter pump. A (heated) rubidium reservoir releases a rubidium influx into the evacuated chamber. The laser beam exits the glass fiber cable to be split in two and guided both through the chamber and through a hollow core fiber to finally be detected on photodiodes. The legend of figure 2.1 also holds for this sketch.

## 2.1. Optical setup in the pyrex glass cell sector

As a laser light source, a distributed feedback laser diode[1] that operates at a wavelength of $780nm$ with a maximal output power of $80mW$ is used. A Peltier element is integrated in the housing for a fast temperature stabilization keeping the system at room temperature ($20°C$) where an integrated thermistor (NTC type) is used as a temperature gauge; the emitted frequency can be precisely tuned by choosing the forward current of the laser diode. Both temperature (in form of the thermistors resistance) and forward current are displayed on controllers that guarantee stable laser operation.
A frequency generator[2] with a triangular voltage output is connected to the current controller in order to linearly change the laser frequency and thus sweep across the rubidium $D_2$-line frequency range. The frequency generator signal is also connected to an oscilloscope[3] to work as a trigger.
Once the laser beam exits the diode laser housing, it is reshaped by lenses and passed through optical isolators in order to prevent any laser light from reentering the laser system in the first place. Then, it passes through one of three intensity regulation units consisting of a $\frac{\lambda}{2}$-waveplate and a polarizing beam splitter cube. One of the

[1] eagleyard photonics, EYP-DFB-0780-00080-1500-TOC03-000x, properties at $25°C$: operation wavelength: $(780 \pm 1)nm$, spectral width (FWHM): $2MHz$
[2] datatec, Model: 33522A
[3] Rohde und Schwarz, Model: Hameg HMO724

splitted laser beams is guided into a glass fiber cable[4] and passed to the second block. The other one makes its way through another intensity regulation unit to pass a rubidium filled pyrex glass cell (which is used as a reference line), be focused down by a $100mm$ lens and fall onto a photodiode[5] which is connected to the oscilloscope.

## 2.2. Optical setup in the vacuum chamber sector and vacuum system assembly

In this block, there is on the one hand the vacuum system to be introduced and on the other hand the optical light guidance setup.

### 2.2.1. Vacuum system assembly

The vacuum system consists of a cylindrical vacuum chamber with a length of $(15.0 \pm 0.1)cm$ and transparent windows on both ends to allow the laser light to enter and exit the system. Inside the chamber, many transparent silica capillaries are placed to allow a proper positioning of the hollow core photonic crystal fibers. The latter are inserted into the capillaries and tried to be centered in the longitudinal axis to both have all fiber tips in one plane and leaving the same space between the two fiber ends and the chamber windows. There are six different fiber types with each three different inner wall coatings available, all having a length of $(14.0 \pm 0.2)cm$. The fibers are organized in three rows of different vertical position and six columns of different horizontal position. The fiber's positional organization is shown in 2.3. A more detailed look at the fiber's properties is presented in chapter 3.4. Each column contains fibers of one type, each row contains fibers of the same coating. The fibers are either PDMS-, sol-gel- or uncoated.

The chamber is attached to a rubidium reservoir of roughly $5g$ of solid rubidium. The solid rubidium was originally inserted into a glass ampoule. The latter was broken, after its insertion into a bellows attached to the vacuum system. The rubidium gas influx can be regulated by a valve. Moreover, there are heating wires wrapped around the reservoir compartment that heat up when a current runs through, turning the rubidium reservoir compartment into an oven.
To evacuate the chamber and keep the inside pressure level at the low rubidium vapour pressure at room temperature (about $2 \cdot 10^{-7}torr$ at $20°C$), a turbo pump[6] is attached to the system. The turbo pump can evacuate up to a pressure of more or less $1 \cdot 10^{-9}torr$. A gauge[7] displays the pressure in front of the turbo pump (still inside the evacuation region). As the turbo pump is both noisy and causes mechanical

[4] polarization conservative, singlemode fiber cable PMC 780 with a fixed focus FC/APC connector F230APC780 with a beam diameter of 0.98mm at one focal length from lens
[5] Thorlabs PDA36A-EC silicon detector with switchable gain
[6] Agilent Twis Torr 304FS, Model: X3500-64005
[7] Agilent, Model: FRG-730 Pirani Bayard-Alpert gauge

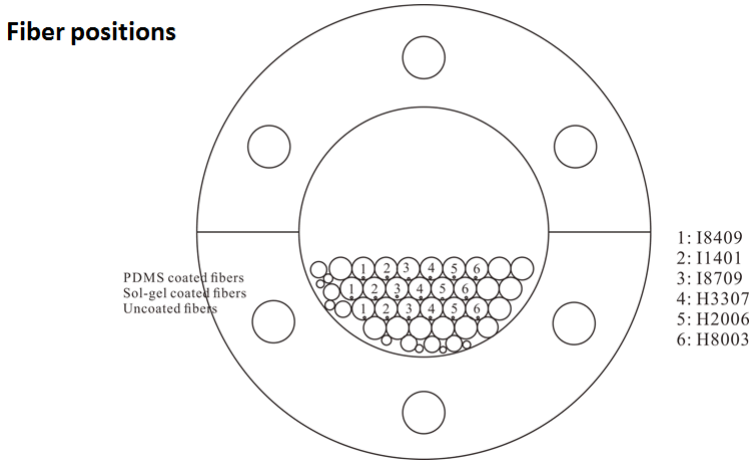


Figure 2.3.: Arrangement of the 18 hollow core fibers inside the vacuum chamber. The front view where the laser enters the chamber is shown. Provided by [20].

vibrations, it is supposed to be used just for initial evacuation. Afterwards, it is meant to be detached. Thus, there is a valve on the way to the turbo pump. Further pumping action is thought to be done by an ion getter pump[8]. The current applied to the ion pump is displayed by a multimeter in form of a voltage. A voltage of $1V$ corresponds to a current of $1mA$. The current then corresponds to a pressure value that yields the evacuation level at the ion pump. The voltmeter is connected to a controller unit[9] that passes on the actual current.

### 2.2.2. Optical setup in the vacuum chamber sector

The laser beam that is branched from the first block to the second block by the glass fiber cable exits it and falls onto the third intensity regulation unit where two beams are created to subsequently pass through the vacuum chamber and the inner fiber structures. One beam is just directed by mirrors through the chamber onto a photodiode[10]. The other beam is furthermore directed by a mirror placed on a horizontally movable stage and focused down by a $100mm$ lens (the lense's choice is presented in chapter 3.2.2). After leaving the chamber, it is also redirected by a mirror to fall onto a photodiode[11]. Before both photodiodes, a $100mm$ lens is placed to focus the beam down to hit the detection area properly. Both photodiodes are connected to the oscilloscope.

[8] Agilent, Model: 9190520, pumping rate: 2l/s
[9] Agilent Minivac, Model: 9290291
[10] Thorlabs PDA36A EC silicon detector with switchable gain
[11] Thorlabs PDA36A EC silicon detector with switchable gain

## 2.3. Additional experimental devices

During the different measurements, two more devices have been used to take both data for the laser beam's power and the beam's transversal profile. In order to measure the laser beam's power, a laser power meter console[12] has been used that produced an analog as well as a digital output. Its power detection capability ranged from $100pW$ to $200W$. The measurable detection range was restricted, depending on the power sensor attached to the console[13] To get information of the beam's transversal extensions, a camera[14] has been used. The camera signal was sent to a computer and analysed by a beam profiler plugin that yielded parameters characteristic for the beam width by fitting a Gaussian profile in both horizontal and vertical direction. The fitting program orientated on intensity peaks that could possibly be identified with the maximal value of a two dimensional error function in the horizontal as well as the vertical axis (corresponding to certain pixel positions) which was also displayed. Further information about the laser beam's transversal beam profile can be found in the chapter 3.1.
The temperature of the laboratory has been measured by a thermostat and was shown on a display device. The temperature has been regulated to keep the room temperature at $20°C$.

[12]Thorlabs, Model: PM100A
[13]Thorlabs, Model : S120C, silicon photodiode sensor, resolution: $1nW$
[14]iDS CCD camera, Model: UI-1540LE

# 3. Laser beam propagation and light guidance through fibers

In this chapter, a short theoretical introduction in laser light propagation is given [21], followed by its experimental verification in form of the Gaussian mode. The light guidance into one and the propagation characteristics behind two fibers are investigated and the lens for the coupling into the 18 fibers inserted in the vacuum chamber is chosen. In the end, there will be taken a closer look at the characteristics of the fibers that are actually placed inside the vacuum system.

## 3.1. Gaussian mode in laser light propagation and its manipulation by optical elements

A laser beam is an electromagnetic wave that is characterized by a propagation direction (here the $z$-axis is chosen as the propagation axis) and a beam intensity distribution that is spatially confined closely to the propagation axis.
Starting with the Maxwell equations in free space and assuming a negligible change in the spatial derivatives of first and second order of the beam's envelope $A(\vec{r})$ (electric field $E(\vec{r},t) = A(\vec{r})e^{-ikz}e^{i\omega t}$) along the propagation axis over one wavelength $\lambda$ (wave vektor $k$) for a monochromatic wave, leads to the paraxial Helmholtz equation:

$$\left(\Delta_{x,y} - 2ik\frac{\partial}{\partial z}\right) A(\vec{r}) = 0 \quad . \tag{3.1}$$

A special solution of the paraxial Helmholtz equation is the so called Gaussian beam, as it has a transversal intensity profile that is described by a normal distribution. Its beam envelope is given by

$$A(\vec{r}) = \frac{A_0^{'}}{q(z)} e^{-ik\frac{\rho^2}{2q(z)}} \ , \ q(z) = z + iz_0 \tag{3.2}$$

where the quantity $q(z)$ is called the $q$-parameter of the beam, $z_0$ is the rayleigh range and $A_0^{'}$ is a complex constant.
In order to clearly separate the amplitude and phase of the envelope $A(\vec{r})$, two new real functions are defined:

$$\frac{1}{q(z)} = \frac{1}{R(z)} - i\frac{\lambda}{\pi w^2(z)} \tag{3.3}$$

with

$$R(z) = z\left[1 + \left(\frac{z_0}{z}\right)^2\right] \ , \ w(z) = w_0\sqrt{1 + \left(\frac{z}{z_0}\right)^2} \ , \ w_0 = \sqrt{\frac{\lambda z_0}{\pi}}\,. \tag{3.4}$$

With all introduced parameters, the electric field for a Gaussian beam can be written as

$$E(\vec{r},t) = A_0\frac{w_0}{w(z)}e^{-\frac{\rho^2}{w^2(z)}}e^{-ikz-ik\frac{\rho^2}{2R(z)}+i\zeta(z)} \tag{3.5}$$

where $A_0 = A_0^{'}/iz_0$ and $\zeta(z) = arctan\left(\frac{z}{z_0}\right)$ is the guoy phase.
In order to find a quantity to define a beam width with finite extend (the electric field does not vanish at any distance from the propagation axis), the beam intensity at a fixed plane $z = const$ can be consulted:

$$I(x^2+y^2,z) \sim |E(\vec{r},t)|^2 = A_0^2\left(\frac{w_0}{w(z)}\right)^2 e^{-\frac{2\rho^2}{w^2(z)}}\,. \tag{3.6}$$

As already mentioned, the intensity profile is governed by a normal distribution with the maximal value on the beam axis. Since the main contribution of the overall beam power (86 per cent) is confined within a circle of radius $w(z)$, $w(z)$ is regarded as the beam radius. As a function of $z$, the beam radius is given by

$$w(z) = w_0\sqrt{1 + \left(\frac{z}{z_0}\right)^2}\,. \tag{3.7}$$

It has its minimum value $w_0$ at $z = 0$ and broadens in both directions on the beam axis likewise asymptotically approaching a linear beam divergence.

Apart from its amplitude and direction of travel, a Gaussian laser beam is completely specified by its $q$-parameter

$$q(z) = z - z^{'} + iz_0 \tag{3.8}$$

where $z^{'}$ is the location of the beam waist on the optical axis. A Gaussian laser beam that falls onto an optical element, keeping its circular symmetry (which requires the optical element to be circular symmetric as well) stays a Gaussian beam which has, however, changed its shape. Its waist size and curvature are modified. Therefore, its $q$-parameter has changed as well. The new $q$-parameter can be easily determined by the ABCD-matrix-formalism. According to this formalism, an optical element's effect on the beam's $q$-parameter can be described by a $2\times 2$-matrix $\begin{pmatrix} \mathrm{A} & \mathrm{B} \\ \mathrm{C} & \mathrm{D} \end{pmatrix}$. The modification of a Gaussian beam's $q$-parameter after passing several optical elements is simply given by multiplying the matrices characterizing the optical elements. The final matrix with the entries $A$, $B$, $C$ and $D$, organized as shown above, changes $q$ in the following way:

$$q_{out} = \frac{Aq_{in} + B}{Cq_{in} + D} \tag{3.9}$$

| | |
|---|---|
| transmission through free space | $\begin{pmatrix} 1 & L \\ 0 & 1 \end{pmatrix}$ |
| transmission through a thin lense | $\begin{pmatrix} 1 & 0 \\ -\frac{1}{f} & 1 \end{pmatrix}$ |
| reflexion from a planar mirror | $\begin{pmatrix} 1 & 0 \\ 0 & 1 \end{pmatrix}$ |
| reflexion from a spherical mirror | $\begin{pmatrix} 1 & 0 \\ -\frac{2}{R} & 1 \end{pmatrix}$ |

Table 3.1.: ABCD-matrices for some optical elements. $L$ represents the passed distance, $f$ the focal length of the lens and $R$ the radius of curvature.

where $q_{in}$ is the former and $q_{out}$ the latter $q$-parameter. In table 3.1, the matrices belonging to a few optical elements are shown.

## 3.2. Laser beam propagation calculations for the glass fiber and a hollow core fiber

Before getting started with the coupling into the fibers inside the vacuum chamber, it is important to know which lens needs to be used in order to optimize the coupling efficiency into the hollow core fibers. Therefore, the shape of the laser light exiting the glass fiber cable is analysed assuming a transversal Gaussian laser mode. Afterwards, the effect of $50mm$, $100mm$ and $150mm$ lenses on the beam's waist radius is calculated. It is desirable to get a beam waist radius at the focal point that is as close as possible to the fiber's mode field radius. Moreover, the propagation of the laser light after the glass fiber transmitting a short hollow core fiber with a length of $l = (9.7 \pm 0.1)cm$ and a mode field diameter of $d = 42\mu m$ is analysed. Both the coupling efficiency for a $50mm$ and a $100mm$ lens and the validity of Gaussian light propagation are tested.
For measuring the beam radius, the camera is placed at different distances along the laser beam axis. The distance measurements are done using a ruler. The camera signal is sent to a computer where a program with a beam profiler plugin calculates the transversal beam profile and yields values for both horizontal and vertical beam radius. A fit to the obtained data is done finding out the relevant beam parameters presented in the theoretical considerations for Gaussian light propagation. The error contributions are given by temporal fluctuations of the laser beam's intensity (which could directly be seen by fluctuations of the calculated beam radius by the beam profiler plugin), a potential pixel size error for the pixels of the camera (pixel size of $5.2\mu m$), one pixel size at the each border of the beam's radius where the fit is done and a deviation from a perpendicular alignment of camera surface and beam propagation axis. The misalignment contribution is negligible compared to the others and consequently not further considered. As the used beam profiler plugin for

calculating the beam radius is not known to be working correctly, the proper working of the program is tested in the first place.

### 3.2.1. Beam profiler test

For testing the results obtained by the plugin program, the camera is placed at a certain distance from the outcoupling position of the laser out of the glass fiber. The plugin results for the beam radius are compared with the results of the camera output signal analysed with python. The camera output signal yields a two dimensional array of numbers in an arbitrary unit for the beam intensity using only integers. As on the edges of the camera's detection surface, far from a clear intensity signal, there is a rather constant, nonzero intensity registrated, this offset (2 a.u.) is taken as the signal's error. Assuming that the beam profiler plugin is oriented on the highest intensity values for the horizontal and vertical axis (which could be seen on an image file the computer program has opened automatically), the same is done in the python analysis. (There have been several maxima, but as they have been located extremely close together, one was arbitrarily chosen). The function used for fitting is given by

$$f(x) = a \cdot e^{\frac{(x-\mu)^2}{2\sigma^2}} + c. \tag{3.10}$$

The beam profiler test yielded the following results:

beam profiler plugin calculation for the beam radius:
horizontal beam radius: $w_0 = (592 \pm 9)\mu m$, vertical beam radius: $w_0 = (610 \pm 9)\mu m$
python calculation for the beam radius:
horizontal beam radius: $w_0 = (591 \pm 8)\mu m$, vertical beam radius: $w_0 = (601 \pm 8)\mu m$

As it can be seen, both calculations lead to results that coincide well within the error range. Thus, the proper working of the beam profiler plugin can be taken for granted. In figure 3.1, the transversal intensity distribution of the beam at the analysed distance from the outcoupler of the laser beam out of the glass fiber can be seen in both a contour plot and a 3D-plot. Figure 3.2 shows the horizontal and vertical intensity distribution at the analysed fixed pixel positions including a plot of the fit function. The figures and fits confirm a clear domination of the Gaussian mode for the laser beam after transmitting the glass fiber.

### 3.2.2. Beam propagation calculation behind the glass fiber

In the following, the beam propagation parameters for the laser beam that will afterwards be coupled into the hollow core fibers is calculated as well as the needed focal length of the lens for beam focussing.

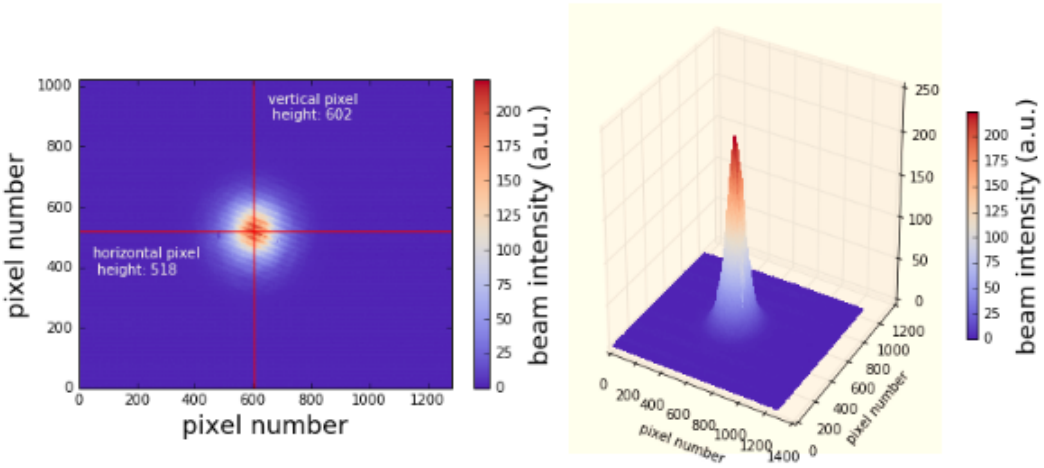


Figure 3.1.: Contour plot of the recorded beam signal's intensity distribution with horizontal and vertical fit positions (left) and 3D-plot of the transversal intensity distribution (right) of the laser beam at a certain distance of the glass fiber's exit location. The intensity distribution is used in order to test the proper working of the unknown used beam profiler plugin for beam waist radius calculation.

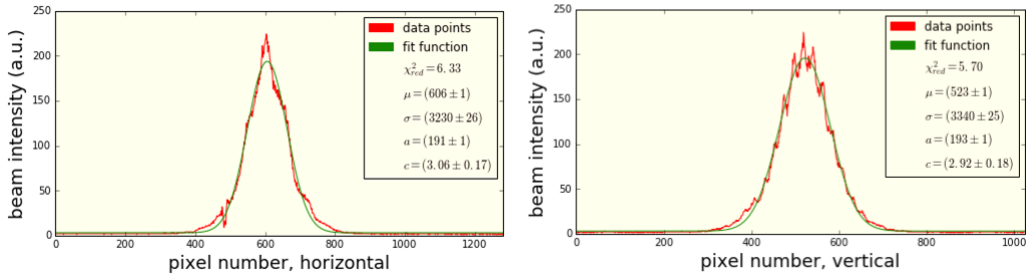


Figure 3.2.: Intensity distribution and Gaussian fits of the laser beam behind the glass fiber at the pixel positions shown in figure 3.1 which have been done with python.

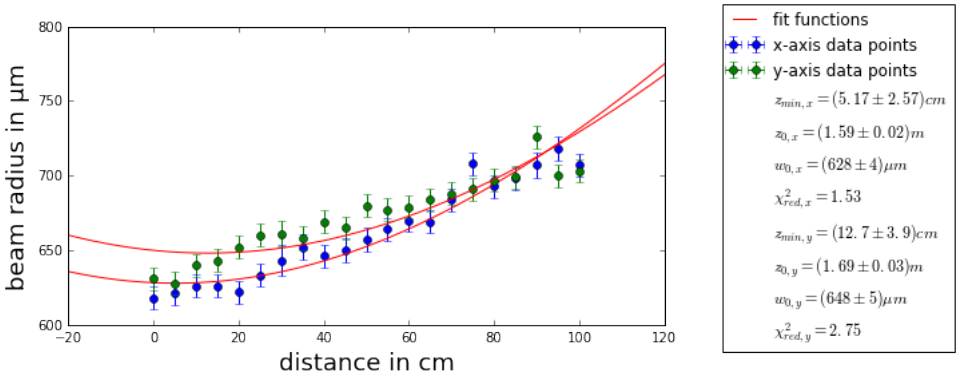


Figure 3.3.: Spatial beam radius evolution of the laser beam exiting the glass fiber for both horizontal and vertical beam axis, including the fit functions for the beam propagation of the Gaussian mode.

Figure 3.3 shows the horizontal and vertical spatial evolution of the laser beam exiting the glass fiber together with fit functions of the form

$$w(z) = w_0 \sqrt{1 + \left(\frac{z - z_{min}}{z_0}\right)^2} \tag{3.11}$$

as presented in the chapter 3.1. The data show a clear rise in beam size with increasing distance for both horizontal and vertical axis, although only the x-axis data show a visible change in beam curvature in the region of the beam waist. Nevertheless, both horizontal and vertical beam radii change likewise alongside the beam's propagation direction which yields the main information for the rayleigh range $z_0$. It can be seen that the beam radius increases within one meter distance of its waist location about 10 per cent of its radius for both transversal directions. While the intensity profile of the laser clearly showed a Gaussian intensity distribution, the expected beam radius evolution does not seem to represent the data very well for the beam propagation obtained behind the glass fiber.
In order to calculate which lens should be used to focus down the laser beam to approach half of the fiber's mode field diameter, two parameters are relevant: the rayleigh range $z_0$ and the distance $L$ that lies between the position of the lens and the beam waist position at $z_{min} = 0$. As can be seen in the legend box of figure 3.3, the rayleigh ranges and beam waist positions for the horizontal and vertical transversal beam evolution are not equal within their errors, but show a larger derivation from one another. Nevertheless, this differences turn out to be of a rather small impact on the lenses' choice which is outlined shortly. Thus, the two rayleigh ranges are averaged to yield $\bar{z_0} = (1.64 \pm 0.04)m$. To get an estimate of $L$, the beam waist positions are also averaged which leads to $\bar{z_{min}} = (8.9 \pm 4.7)cm$. The laser beam evolution has not been measured directly behind the light outcoupler attached to the

glass fiber, but at a certain distance from it where even two mirrors have been placed in between. The distance value of $0cm$ corresponds to a position somewhere behind the two mirrors. The situation is similar in the optical setup shown in figure 2.2 where two mirrors and additionally a $\frac{\lambda}{2}$-waveplate as well as a pbs-cube are located in between the lens and the position of the outcoupler. Their influence on the beam propagation is neglected and has not been found to be significant by measuring the beam sizes in front of and behind the devices with the camera. $L$ is as a consequence simply the difference of the lenses' position and the beam's waist position with respect to the outcoupler's location. The beam's waist position can be calculated with the beam propagation measurement. The lenses' position can also be measured. Both distance measurements have been carried out by using a ruler. Finally, $L$ is calculated to be $(17 \pm 7)cm$.
As all relevant parameters have been calculated, the ABCD-matrix formalism can be applied. The incident laser beam falling onto the lens has a $q$-parameter of $q_{in} = L + iz_0$. The lens is taken to be thin enough for justifying its modelation by the matrix shown in table 3.1 for a thin lens. Its extension alongside the beam propagation axis is about two orders of magnitude smaller than the incoming beam's rayleigh range and about one order of magnitude smaller than the outgoing beam's rayleigh range. The new $q$-parameter is therefore given by

$$q_{out} = \frac{q_{in}}{1 - \frac{L}{f} - i\frac{z_0}{f}}. \tag{3.12}$$

The imaginary part of the new $q$-parameter yields the information for the beam waist radius that is reached within the distance of one focal length $f$ behind the lens. It is given by

$$\Im(q_{out}) = \frac{z_0 f^2}{z_0^2 + (f - L)^2} \tag{3.13}$$

where $z_{0,new} = \Im(q_{out})$. Since the square of the former rayleigh range $z_0^2$ is much larger than $(f - L)^2$, the large uncertainty of $L$ does not play too much of a role and is even less significant than the error contribution of $z_0$. The uncertainty of the focal length of the three lenses analysed (focal length of $50mm$, $100mm$ and $150mm$) is taken to be $\Delta f = 1mm$. The error of the new rayleigh range $z_{0,new}$ is obtained by adding up all three independent error contributions. The results obtained for all three lenses and the beam waist radii $w_0 = \sqrt{\frac{z_{0,new}\lambda}{\pi}}$ are shown in table 3.2.
Although the approximation of the lenses to be treated as thin and therefore use the matrix for thin lenses to the incoming beam's $q$-parameter has not been taken into account, it can be seen that the $100mm$ lens should work best for most of the fibers. The mode field radius of the fibers is obtained by multiplying their inner radius (which is shown in figure 3.6 in 3.4) with $\frac{\pi}{4}$ (private communication with [20]). It is represented best by the beam waist of nearly $40\mu m$ of the $100mm$ lens. Only for the fiber type H8003, it would be convenient to change to the $150mm$ lens. As it is difficult to exactly place the lens at one focal length of a fiber tip, it is useful to know,

| focal length of lens | rayleigh range in $mm$ | beam waist radius in $\mu m$ |
|---|---|---|
| $50mm$ | $(1.52 \pm 0.04)$ | $(19.4 \pm 0.3)$ |
| $100mm$ | $(6.09 \pm 0.14)$ | $(38.9 \pm 0.5)$ |
| $150mm$ | $(13.72 \pm 0.35)$ | $(58.4 \pm 0.8)$ |

Table 3.2.: Rayleigh ranges and beam waist radii of the Gaussian beam after the transmission through three different thin lenses for the incoming beam that originated from the glass fiber outcoupler.

how fast the beam radius changes close to its waist location. For the $100mm$ lens, the beam radius rises about 15 per cent within a deviation of $2mm$ of the waist location.

## 3.3. Analysis of the additional hollow core fiber

At last, the propagation of the laser light behind the glass fiber passing through the short hollow core fiber with a length of $l = (9.7 \pm 0.1)cm$ and a mode field diameter of $d = 42\mu m$ is analysed. Both the coupling efficiency for a $50mm$ and a $100mm$ lens and the validity of Gaussian light propagation are tested in the following.
The fit function for the beam radius evolution is again given by

$$w(z) = w_0 \sqrt{1 + \left(\frac{z - z_{min}}{z_0}\right)^2}. \tag{3.14}$$

The data and the fits for the beam propagation for the $50mm$ and $100mm$ lenses behind the fiber are shown in figure 3.4.
In comparison with the data obtained for the beam radius evolution behind the glass fiber, apparently no longer the error contribution of the beam radius, but rather the error contribution for the distance measurement is more relevant. This is the result of a much quicker change in the beam radius in a much shorter distance for the hollow core fiber. The data points taken behind the hollow core fiber tip are all located in the region where the beam divergence does not differ much from its asymptotic limit anymore unlike for the beam behind the glass fiber. Thus, they are more or less located on a straight line. In comparison with the observations made for the beam radius evolution behind the glass fiber, the beam radius evolution behind the hollow core fiber can be described well by the expected parametrisation, even though only the asymptotic behaviour could be recorded in this case.
For the $50mm$ lens, the horizontal and vertical beam evolution is quite similar in comparison with the $100mm$ lens. The differences between horizontal and vertical radius evolution of the $100mm$ lens could not be minimised more. The coupling has been done as good as possible. The large difference of the beam radius evolution for the horizontal axis of the $100mm$ lens should arise from a misalignment between fiber and beam propagation direction or a non central light entrance into the fiber,

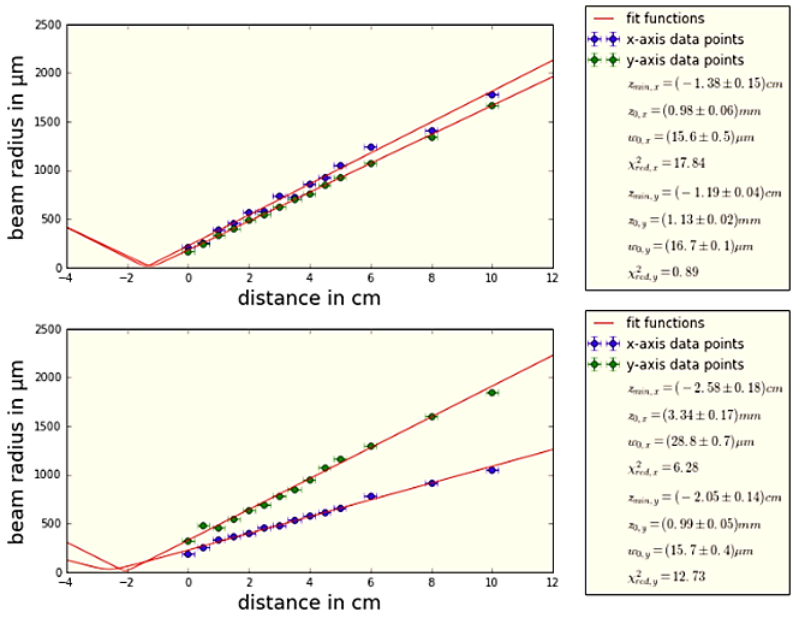


Figure 3.4.: Beam radius evolution together with the fit functions behind the additional fiber (mode field diameter $42\mu m$). Both a $50mm$ (top) and $100mm$ (bottom) lens have been used for the coupling.

although the camera showed in both horizontal and vertical direction a Gaussian intensity distribution. Moreover, there was paid attention not to enter the intensity saturation limit of the camera in order to guarantee a good fitting procedure for the beam profiler plugin. Furthermore, the data for the $50mm$ lens do not show the same deviation as the data for the $100mm$ lens which indicates that the hollow core should have a rotation symmetry at the tip. The deviation might also be explainable by the observation that the $50mm$ lens is the better one to be chosen for this hollow core fiber whose radial dimensions are only about half of those of the fibers inside the vacuum chamber. The beam waist radius is about $15 - 17\mu m$ large (not considering the x-axis data of the $100mm$ lens) and therefore close to the value calculated earlier for the focussing power of the $50mm$ lens in front of the vacuum chamber which is shown in table 3.2. At last, there is to mention that for both axis in each plot the $z_{min}$ location should coincide, since it represents the fiber's tip position. Considering the difference of the values for both axis in both plots, there is drawn the conclusion that the deviations of this fit parameter is just the result of the data points not being located exactly on a straight line.
The mode field radius of the fiber is said to be $21\mu m$ and thus larger than the waist radii calculated. As the calculated values are about $71 - 81$ per cent of the size of the given value and the data points as well as the unknown pixel size error of the camera are thought to allow for a certain variation of the beam divergence, the paraxial

approximation is still considered to yield a good description of the beam propagation, although close to the limit of its application range. The wavelength of the laser is about 5 per cent of the beam waist radii occuring here and thus not to be neglected completely anymore.
The coupling efficiencies were found to be $(62 \pm 2)$ per cent for the $100mm$ lens and $(75 \pm 2)$ per cent for the $50mm$ lens. This is consistent with the $50mm$ lens to be the better choice for an optimization of the coupling efficiency for the given fiber. Having in mind that within the beam radius of a Gaussian mode 86 per cent of the total power is contained, there should consequently not be to much of the light going into the fiber core for the $100mm$ lens in the first place. Therefore, there is much light entering either the fiber's cladding structure and the outer glass coating. This light could be scattered away in the end. Also a non optimal lens placement reduces the coupling efficiency.
As for the fiber analysed here, the laser beam waist for the $50mm$ lens and the mode field radius of the fiber have similar proportions compared to each other than in the lens-fiber system of the vacuum and optics setup of the main experiment where the absolute values for the radii are roughly doubled, there will be made a comparison with the coupling efficiency of $(75 \pm 2)$ per cent for the $50mm$ lens obtained here.

## 3.4. Hollow core photonic crystal fiber properties

Hereinafter, a closer look on the fibers inside the vacuum chamber is given. As the fibers are supposed to be characterised with respect to the question on how suitable each one of them is to be chosen as an ideal gas host and waveguide system, it is considered useful to discuss their specific properties in more detail.

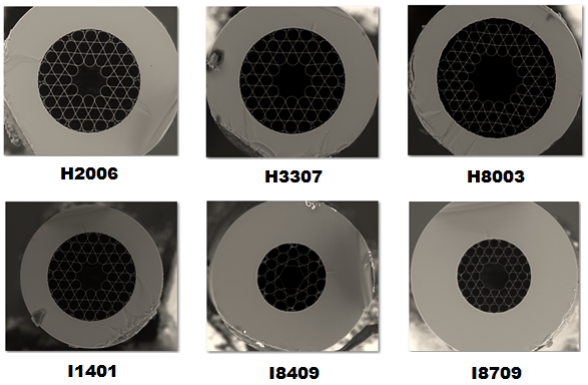


Figure 3.5.: Transversal profile of the six different fiber types inside the vacuum chamber. Provided by [20].

The fibers used in the scope of this experiment have all roughly a length of $l =$

$(14.0 \pm 0.2)cm$. There has not been a measurement performed of the length of the fibers. Their longitudinal extension has been estimated by orientating on the vacuum chamber length and the distances of the fiber tips from the chamber windows. The transversal structure of the fibers is subdivided into three components: the hollow core in the center, a wb/lattice-like cladding (Kagome type) that encircles the hollow core and an outer coating surrounding the cladding structure. The overall transversal shape is circular. The transversal structure for the six different fiber types available is plotted in figure 3.5.
It can be seen that the fiber core is not circular for any fiber but has a hexagonal kind of shape which is different for all fibers. Therefore, there an inner and an outer core radius is given for each fiber. The core is then surrounded by the Kagome cladding that consists of many cells whose form differ from fiber to fiber. The cladding is then ultimately encased by an outer coating. The proportions of these three segments are also varying from fiber to fiber to result in an overall radial extension of roughly $300\mu m$.

| | Cells | Rin/Rout | OD | Curvature *b* | Loss@480nm | Loss@780nm | MFD |
|---|---|---|---|---|---|---|---|
| I8409 | 1 cells broadband | 41.6um/47.6um | 300 um | / | 630 dB/km | 170 dB/km | |
| I8709 | 7 cells broadband | 49.8um/53.8um | 315 um | 0.49 | | 35 dB/km | |
| I1401 | 7 cells | 47.0um/58.5 um | 270 um | 0.93 | | | |
| H8003 | 19 cells | 85.4um/102.2um | 330 um | 0.98 | | 500 dB/km | |
| H2006 | 7 cells | 52.2um/65.1um | 350 um | 0.99 | 600 dB/km | 300 dB/km | |
| H3307 | 7 cells | 58.8um/71.2um | 325 um | 0.94 | | 430 dB/km | |

Figure 3.6.: Data for the six different fiber types available in the experiment. Provided by [20].

Additional information about the individual fiber types is provided in 3.6. The light loss for a $780nm$ laser beam transmitting the fibers is also shown. The loss for the short fibers in this experiment is very small. For all of the fibers, the loss is equal to or smaller than $0.07dB$. This corresponds to a loss of roughly 1.6 per cent in beam power.

In figure 3.7, three different levels of light coupling into the fiber type H8003 are shown. White coloured spots indicate saturation which allowed a better visualization of how the light exiting the fiber distributes. In the leftmost picture, the light exiting the fiber underlies strong scattering. This could also be seen on both fiber tips for high enough beam intensity by a red light flash on each tip. The circular shape of the overall light spots gives a hint that light is entering the fiber. In the central picture, the coupling is further improved. It illustrates the hexagonal kind of shape of the fiber core and cladding structure where light is observed to gather in six clusters all around the hollow core. Also some light comes out of the core. In the rightmost picture, the coupling has been optimised. The picture clearly shows that the beam intensity is concentrated in the hollow core. The camera affirms a Gaussian intensity distribution for both horizontal and vertical axis for such an optimized coupling level not only for

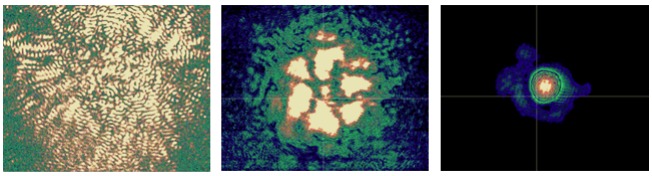

Figure 3.7.: Illustration of three different levels of fiber coupling for the fiber type H8003. The coupling improves from left to right. As the position of the beam intensity maximum and the beam's direction are adjusted to match the fiber core's position and the fibers longitudinal alignment, the light scattering reduces to finally yield a Gaussian intensity distribution propagating through the fiber.

this but for each fiber type.
Up to now, the focus has been put on the waveguiding properties of the fibers. There are as well efforts done in fiber fabrication to reduce surface interaction effects which modify the spectral properties of vapours filled inside. The fibers are all made out of silica material. Thus, gas particles inside a hollow core fiber are underlying physisorption and chemisorption effects in a silica material environment. As the vapour pressure for rubidium at room temperature is extremely low (roughly $2 \cdot 10^{-7} torr$ at $20°C$), there are basically no atom-atom interactions taking place but rather only atom-surface interacions. In order to minimise unwanted modifications in light-matter interactions for light guided through the fibers, the silica surface surrounding the hollow core is covered with a thin film of another material. The procedure of covering the inner core wall of a fiber is explained in [19], in the case of further interest. There have been many different kinds of material used as coatings for the inner core walls, as for example PDMS, aluminosilicate sol-gel, paraffin and sapphire.
The fibers in this experiment are either uncoated or PDMS/sol-gel coated. The PDMS coating is chosen for its desirable antirelaxation and light atomic induced desorption properties. Sol-gel coatings can have a diverse range of physical properties, as a consequence of the range of precursor chemicals that can be used for the wet solution that is further processed to sol-gel. The choice for this material is further motivated by its high corrosion resistance [19].
As already mentioned, the vapour pressure of rubidium is extremely low at room temperature and therefore the rubidium migration inside a hollow core fiber is mainly determined by surface interactions. Thus, the choice of an appropriate interaction surface does not only have an impact on the spectral properties of rubidium but also on the diffusion of atoms into/inside the fibers.

# 4. Diffusion calculations and observations for rubidium atoms filling hollow core fibers

In this chapter, the diffusion process of rubidium atoms making their way into the different hollow core fibers inside the vacuum chamber is analysed. The pressure inside the chamber is considered to be in the range of the vapour pressure of rubidium at room temperature, once steady state conditions have been reached. As a consequence of the low vapour pressure rubidium has under these conditions, the migration process of rubidium into the fibers is not governed by atom-atom interactions anymore, but rather by the surface interaction between the atoms and the fiber's cladding material. It is known that it can take a lot of time for atoms or molecules to fill host structures like the hollow core fibers whose diameter (about $80\mu m - 210\mu m$) is small compared to their length (about $14cm$)[22,23]. The time scale can reach from hours to months to get a relatively high particle density along the entire fiber length compared to the outer particle density and therefore there is a need to wait until the filling process is completed to start analysing the spectral properties of rubidium atoms inside the fibers.
It is thus tried to get a coarse estimate on the scale of the period of time needed for the filling process by applying the one dimensional diffusion equation for a free particle flow into a cylindrical tube with a silica material/ PDMS or sol-gel coated surface whose radius is extremely small compared to its overall length. In the end, the experimental observations are presented.

## 4.1. Regimes of gas particle flow

For the description of the evolution of a given gas particle distribution in space within a certain boundary structure, there exist three regimes: the viscous, the slip flow and the molecular flow regime [24]. In each of them, different interactive processes determine the ongoing gas particle flow. Which regime has to be chosen for a specific problem depends on the so called Knudsen number $K_n$. It is simply given by the ratio of the particle's mean free path $\Lambda$ for particle-particle collisions and a representative length $L$ for the dimension of the surrounding structure of the gas particles: $K_n = \frac{\Lambda}{L}$. In the viscous flow regime, the flow of gas particles is the result of particle collisions. Interactions with each other occur much more often than interactions with surrounding wall material. The wall material influences therefore can be seen in friction effects that slow particles down and create a velocity gradient in perpendicular direction.

Most of the particles are located in between the surrounding environment and are thus not sticking to it. The Knudsen number is therefore much smaller than 1.
In the molecular flow regime, particle collisions with the surrounding walls are much more likely to happen than particle-particle interactions. The overall macroscopic particle movement underlies a more statistical behaviour. Moreover, the main processes governing the particle flow are given by interactions with the surrounding materials. The adsorption-desorption dynamics play an important role, as most of the particles will be found to be stuck on surrounding materials in a steady state condition. The Knudsen number is much bigger than 1 in this case.
The slip flow regime is a transition region where a particle will hit more or less likely the wall than another particle. The particle flow can be described as a superposition of the two regimes already mentioned with an increasing domination of the regime the actual flow problem is closer to. The Knudsen number is close to 1.

For rubidium atoms moving inside the given vacuum chamber entering the hollow core fibers, the molecular flow regime is appropriate for describing the diffusion process. For gas atoms, the mean free path $\Lambda$ is given by [25, page 196]:

$$\Lambda = \frac{1}{n\sigma} \tag{4.1}$$

where $n$ is the particle density and $\sigma$ the particle-particle collision cross section. Using the ideal gas law and modeling the cross section area by treating the rubidium atoms like small solid balls with a fixed radius results in:

$$\Lambda = \frac{kT}{4\pi r_{Rb}^2 p} \tag{4.2}$$

with $n = \frac{p}{kT}$ and $\sigma = \pi(r_{Rb} + r_{Rb})^2$ where $k$ is the Boltzmann constant, $T$ is the temperature, $p$ is the gas pressure and $r_{Rb}$ is the rubidium atom radius. This yields at room temperature $T = 293.15K$, the vapour pressure of rubidium $p = 2.1 \cdot 10^{-7} torr$ at room temperature (see figures A.1 and A.2 in the appendix) and with an atomic radius of $r_{Rb} = 235pm$ [26] a mean free path of $\Lambda \approx 208m$ which is much bigger than the fiber core diameters ($80\mu m - 210\mu m$) and as a consequence a Knudsen number in the order of $K_n = 10^6 - 10^7$ is calculated.

## 4.2. Fick's law with an appropriate diffusion coefficient

For diffusion processes, the driving mechanism for particle flow is particle density fluctuations. Where the particle density is higher, there are more collisions taking place than in a region with a lower particle density. Therefore, a particle is transported from a region of higher particle density to a region of lower particle density simply out of statistical probability reasons. The net flow of particles is described by Fick's law [25, page 201]:

$$\vec{j} = -D \cdot \nabla(n(\vec{x}, t)) \tag{4.3}$$

where $\vec{j}$ is the particle flow rate per unit time and unit area, $D$ is the diffusion coefficient and $n$ is the particle density.

The difficult task here is to find the correct diffusion coefficient for the filling process of the hollow core fibers at the low vapour pressure values of rubidium atoms at room temperature. Thus, an approach developed by P.Clausing [27,28] is motivated in the following and used for the diffusion calculation carried out later on. In this approach, the free molecular flow regime is considered for the diffusion process into a cylindrical tube whose diameter is negligible as compared to its length. The diffusion coefficient calculated there is found to be given by

$$D = \frac{4}{3} \frac{r_{tube}^2}{\frac{2r_{tube}}{\bar{v}} + \tau_a} \tag{4.4}$$

where $r_{tube}$ is the tube's radius, $\bar{v}$ is the mean gas particle velocity and $\tau_a$ is the mean adsorption time on the tube walls whenever there is a wall collision taking place.
For particles just moving in free space, the diffusion coefficient is given by [25, page 201]

$$D = \frac{1}{3} \Lambda \bar{v} \,. \tag{4.5}$$

Thus, the diffusion coefficient is pressure dependent, since the mean free path is a function of gas particle pressure. For being deep in the free molecular flow regime where no gas particle interactions take place, the mean free path is limited by the tube's diameter. As the spatial distribution of further movement of particles after hitting the tube wall at any angle (this also holds for a desorption process of the wall) is weighted by a cosine function, the diffusion coefficient comes out to be

$$D = \frac{1}{3} 2 r_{tube} \bar{v} \,, \tag{4.6}$$

assuming that the wall just acts as a reflective boundary. This type of diffusion where no sticking to the wall takes place, is called Knudsen diffusion. It can be seen that the pressure dependence of the diffusion coefficient vanishes. This can be justified by the fact that there is a lack of inter-particle communication, as there are nearly no gas particle-particle collisions, and by an equal scaling of the particle number entering the tube for a given outer particle pressure and the number of particles needed to completely fill the tube. The last result for the diffusion coefficient is also obtained by setting $\tau_a = 0$ in Clausing's diffusion coefficient. Taking into account adsorption and desorption effects as well with the mean adsorption time $\tau_a$, leads to Clausing's diffusion coefficient.
What has still not been mentioned is that this diffusion coefficient only yields an approximate value for the diffusion coefficient in [28]. In the exact formula, there is a weight factor for $tau_a$ reducing its influence. The model makes use of the so called Langmuirian adsorption. Therein, the whole surface of the tube is divided into cells, each of which can be filled by incoming particles. If a particle hits a cell already

occupied by another particle, it is simply reflected and thus not adsorbed by the wall. This leads to an effective loss of adsorption power, once there are already many particles stuck onto the wall. This considers the fact that particles stuck on the tube wall can reenter the inner part of the tube leaving the wall by desorption. Reaching a steady state condition, the number of particles sticking to the wall per unit time and unit area matches the number of particles leaving the wall per unit time and unit area. Therefore, it makes no difference to have either a particle stick to the wall while at the same time another particle leaves the wall at the same place or a particle just being reflected when hitting the wall. As a consequence, the diffusion will then be again the same as in the case of Knudsen flow.
It is stated in [28] that, for being deep inside the free molecular flow regime and thus having very low particle pressures, this effect can be neglected which results in a time and space independent diffusion coefficient that is used in the upcoming calculations. In order to get an estimate of how long it takes for Langmuirian adsorption to become relevant, a small calculation is done.
The number of gas particles $\mathrm{d}N$ making their way through the surface element $\mathrm{d}A$ in the time period $\mathrm{d}t$ out of the solid angle $\mathrm{d}\Omega$ at the polar angle $\theta$ at a given particle density $n$ is given by [25, page 201]:

$$\mathrm{d}N = nf(v)\mathrm{d}v\mathrm{d}Acos(\theta)\frac{\mathrm{d}\Omega}{4\pi}\,. \tag{4.7}$$

$f(v)$ is the Maxwell-Boltzmann velocity distribution. Dividing this equation by $\mathrm{d}t$ and integrating both over the velocity distribution and a solid angle of $2\pi$, as only gas particles incoming from a total solid angle of half a sphere can enter the fiber from the outside, as well as substituting $\mathrm{d}A$ with the entrance area $2\pi r_{fib}^2$ yields for the number of particles per unit time entering the fiber:

$$\frac{\mathrm{d}N}{\mathrm{d}t} = \frac{\pi}{2}n\bar{v}r_{fib}^2\,,\ \bar{v} = \sqrt{\frac{8kT}{\pi m}} \tag{4.8}$$

Assuming that the number of gas particles $N$ needed to fill the fiber is given by $N = nV = nl\pi r_{fib}^2$ and just considering particles entering the fiber (which is an underestimation of the actual filling time interval), the time interval $\Delta t_{fill}$ for filling the entire fiber is given by:

$$\Delta t_{fill} = \frac{N}{\frac{\mathrm{d}N}{\mathrm{d}t}} = \frac{2l}{\bar{v}} \tag{4.9}$$

For $^{85}Rb$ atoms with an atomic mass of $m = 84.912u$ at $293.15K$ and a fiber length of $l = 14cm$, the time interval comes out to be $\Delta t_{fill} = 1.04ms$.
The time interval $\Delta t_{cover}$ needed to get one layer of rubidium atoms along the entire fiber length just considering the particle number per unit time $\frac{\mathrm{d}N}{\mathrm{d}t}$ entering the fiber that has just been calculated is very long in comparison:

$$\Delta t_{cover} = \frac{\frac{0.907\cdot 2\pi r_{fib}l}{\pi r_{Rb}^2}}{\frac{\mathrm{d}N}{\mathrm{d}t}} \approx 9.3h \tag{4.10}$$

where the factor 0.907 is due to the closest packing of equal spheres in two dimensions; the radius of rubidium atoms is taken to be $r_{Rb} = 235pm$ again and for the fiber radius the average of inner and outer core radius of the thinnest fiber $\bar{r}_{fib} = 44.6\mu m$ where the wall occupation takes the shortest time has been inserted. In order to calculate the particle density, the ideal gas law has been used with the vapour pressure of rubidium at $T = 293.15K$.
As will be outlined later on, the typical filling times for the available fibers are in the order of a few days. Thus, Langmuirian adsorption certainly plays a role after all, accelerating the diffusion process. The calculated filling times are therefore representing upper time limits with respect to the influences of Langmuirian adsorption.
For the calculation of the diffusion coefficient, the only missing component is the average adsorption time $\tau_a$. It can be calculated using an Arrhenius expression [29]:

$$\tau_a = \rho\tau_0 e^{\frac{E_a}{kT}} \tag{4.11}$$

where $E_a$ is the adsorption energy barrier which needs to be overcome for a desorption process. The prefactor $\tau_0$ represents the number of attempts per unit time of an adsorbed particle to break free. $\rho$ is the sticking probability. The reciprocal value of $\tau_0$ is in the order of the lattice oscillation frequency of the adsorbant. Unfortunately, there has not been any experimental calculation/measurement of $\tau_a$ found for the fiber silica material, but only for $E_a$ which is usually measured by light induced atomic desorption processes [30]. The only reference source found for getting a value for the sticking probability $\rho$ is [31] where it is taken to be close to 1 as a consequence of the high rubidium reactivity with glass. Therefore, $\rho = 1$ is assumed. A much smaller sticking probability would result in a much smaller filling time. This leaves the exponential prefactor unknown. For dielectric materials, it is supposed to be more or less in the order of $10^{-13}s$ [29] which will therefore be used for the evaluation of the diffusion coefficient $D$ for a silica surface. As natural rubidium is composed of two different isotopes, the process of diffusion will not take the same amount of time for both of them. The diffusion will take slightly longer for the heavier isotope. But as the shift that results out of the different isotope masses is relative small, it is not changing the diffusion coefficient at all compared to other error contributions which is shown in the following. The diffusion coefficient ranges are shown in table 4.1 for the six different fiber types placed inside the vacuum chamber. As the hollow core of the fibers is not circular (there is an inner and outer radius given for the central opening, see figure 3.6), the two values for the core radius have simply been averaged. The temperature inside the chamber is assumed to be $T = 293.15K$ ($20°C$, room temperature), the adsorption energy is given by $E_a = (0.66 \pm 0.02)eV$ [30] and the exponential prefactor is taken to be $\tau_0 = 10^{-13}s$ yielding an average adsorption time of $\tau_a = (22\pm^{28}_{12})ms$. The large uncertainty arises from the error of the adsorption energy whose contribution scales exponentially. The value for the adsorption time is the dominant contribution in the denominator of the equation for $D$. Consequently, the absolute value of the diffusion coefficient scales inversely with respect to $\tau_0$. Since the prefactor $\tau_0$ causes the main error contribution, a detailed error calculation is not done.

| fiber type | radius $\bar{r}_{fib}$ in $\mu m$ | diffusion coefficient range in $10^{-8}\frac{m^2}{s}$ | filling time range in $h$ |
|---|---|---|---|
| I8409 | 44.6 | 5.3-26.5 | 72-359 |
| I8709 | 51.8 | 7.2-35.8 | 53-264 |
| I1401 | 52.8 | 7.4-37.2 | 51-257 |
| H2006 | 58.7 | 9.2-45.9 | 41-206 |
| H3307 | 65.0 | 11.3-56.3 | 34-168 |
| H8003 | 93.8 | 23.5-117.3 | 16-81 |

Table 4.1.: average radius, diffusion coefficient and filling time ranges for the six hollow core fiber types available for a glass material cladding

The results for $D$ are therefore just an estimate of the order of magnitude of where the diffusion coefficient should be located and as a consequence also the time needed for the fiber filling. The filling time can be calculated by solving the one dimensional diffusion equation which is done in the upcoming section. Its range is also shown in table 4.1. A fiber is viewed as filled, once the particle density alongside the whole fiber has exceeded 85 per cent of its final value which is approached asymptotically over time.

## 4.3. The diffusion equation and its analytical solution

Using Fick's law and combining it with the particle/mass conservation equation (particles are neither created nor destroyed):

$$\frac{\partial}{\partial t}n + div(\vec{j}) = 0\,, \tag{4.12}$$

the evolution of the particle density can be described by the diffusion equation:

$$(\frac{\partial}{\partial t} - D\Delta)n(\vec{x},t) = 0 \tag{4.13}$$

. For the special case of rubidium atoms migrating alongside the hollow core fibers, the diffusion equation reduces to a one dimensional problem: $\Delta = \frac{\partial^2}{\partial x^2}$. This is a homogeneous partial differential equation. As for the diffusion process of rubidium atoms into the fibers only the movement along the fiber axis is relevant, the differential equation reduces to a one dimensional problem concerning the spatial dependence of the particle density.
The one dimensional diffusion process can be solved analytically for any initial condition by a convolution integral [32] :

$$n(x,t) = \frac{1}{2\sqrt{Dt\pi}}\int_{-\infty}^{\infty} n_{initial}(y)\cdot e^{\frac{-(x-y)^2}{4Dt}}\,\mathrm{d}y \tag{4.14}$$

where $n_{initial}$ represents the initial condition. Here, there is assumed a distribution of particles that is in equilibrium in the vacuum chamber outside the fiber, whereas

there are no atoms inside the fiber. The initial condition is therefore given by

$$n(x,0) = n_0(\Theta(x - \frac{l}{2}) + \Theta(-x - \frac{l}{2})) \tag{4.15}$$

where $\Theta$ is the Heavyside function and $l$ represents the fiber length.
The solution of the problem is given by

$$n(x,t) = n_0(1 - \frac{1}{\sqrt{\pi}} \int_{\frac{x-\frac{l}{2}}{\sqrt{4Dt}}}^{\frac{x+\frac{l}{2}}{\sqrt{4Dt}}} e^{-y^2}\,\mathrm{d}y) \tag{4.16}$$

The region that will take longest to fill with rubidium atoms is the center of the fiber. Therefore, the particle density will have a local minimum there for a given point in time which makes it more attractive to just consider the filling of the center over time:

$$n(0,t) = n_0(1 - \frac{1}{\sqrt{\pi}} \int_{\frac{-l}{\sqrt{16Dt}}}^{\frac{l}{\sqrt{16Dt}}} e^{-y^2}\,\mathrm{d}y) \tag{4.17}$$

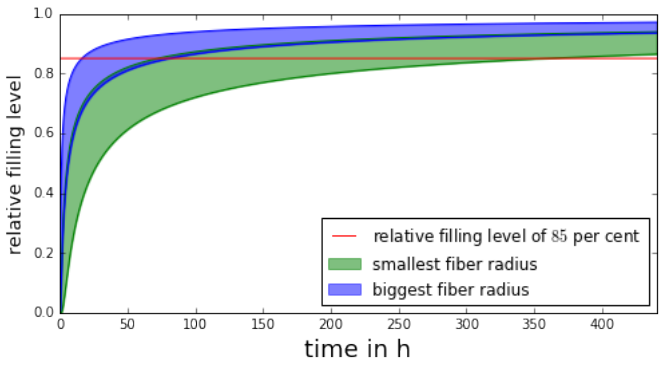


Figure 4.1.: Relative filling level evolution over time for the fiber centers for the fiber with smallest and largest radius for a silica interaction surface. The coloured areas represent the time uncertainty.

It can be seen that the time needed to fill the fiber center scales with the diffusion coefficient $D$. This can already be seen in Fick's law, as the net flow rate of particles increases linearly with $D$ for a given particle density derivative.
Of all six fiber types available in this experiment, the fiber with the smallest radius gives the upper time limit that needs to be waited before performing spectroscopical measurements inside the fibers, because this fiber will take longest to fill with rubidium.
In figure 4.1 the evolution of the relative level of the filling process over time is plotted in the fiber center where the rubidium density has its minimum for both the fiber with smallest and largest radius. The rubidium atom interaction surface is basically silica.

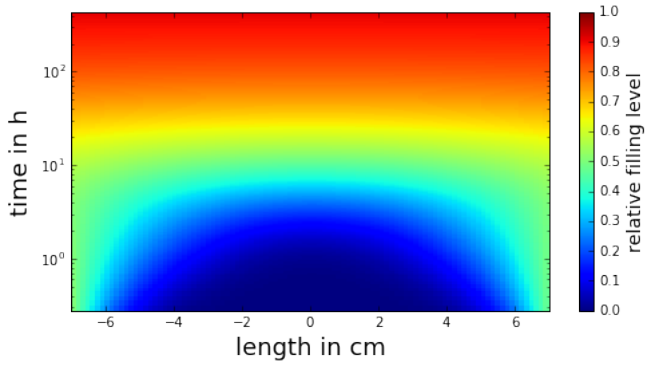


Figure 4.2.: Relative filling level evolution over time along the fiber with smalles radius for a silica interaction surface. The central adsorption time value of $\tau_a = 22ms$ has been chosen to visualize the diffusion process yielding a diffusion coefficient of $D = 12.1 \cdot 10^{-8} \frac{m^2}{s}$.

The coloured areas represent the time uncertainty that is a consequence of the adsorption time range calculated. Also the relative filling level of 85 per cent is plotted which has been taken as a limit to be exceeded for the filling process to be taken as completed. There is a slight overlap in the time ranges for the two fiber types. The crossings with the 85 per cent level are given in table 4.1 for all fiber types. The fiber with largest radius needs about 16-81 hours to fill, whereas the fiber with smallest radius takes about 72-359 hours. Thus, it takes about two weeks to be sure that all fibers are filled with a respectable amount of rubidium atoms.
Figure 4.2 additionally shows the evolution alongside the whole fiber with smallest radius. For this plot, the central adsorption time value of $\tau_a = 22ms$ has been chosen which leads to a diffusion coefficient of $D = 12.1 \cdot 10^{-8} \frac{m^2}{s}$. The relative filling level rises slower approaching the fiber center. The differences in the relative filling level alongside the fiber are largest at the beginning of the filling process and they asymptotically reduce, once the filling level draws close to 100 per cent.
Ultimately, the rubidium atom diffusion process for both a PDMS and sol-gel surface coating are still to be discussed. Recapitulating the conclusions drawn from the form of Clausing's diffusion coefficient, the filling time for the two surface coatings is simply obtained by multiplying the filling time for a silica interaction surface by the ratio of the mean adsorption times, $\frac{tau_{a,PDMS/sol-gel}}{tau_{a,silica}}$. Unfortunately, a reliable source for the adsorption time has neither been found for a PDMS nor a sol-gel coating. But as these materials are installed on the inner fiber walls to strongly reduce surface interactions and consequently unwanted modifications of the spectroscopic properties of gas located inside a fiber, the filling time will be reduced as well. Therefore, according to the presented model, the filling time is smaller for these materials compared to a silica surface. This implies that there is basically no need to wait before performing spectroscopic measurements for the coated fibers.

## 4.4. Accuracy of the diffusion model

In the end, there remains the question on how accurate the obtained results are. Of course, there is already a quite strong limitation given, resulting out of the unknown adsorption time of rubidium on surfaces, but there are other influences that have been neglected in the presented diffusion model.
The used diffusion coefficient which has been derived by P. Clausing assumes that the object to be filled with gas particles is a cylindrical tube with a well defined radius. The radial extension of the hollow fiber cores has minima and maxima with respect to the polar angle. Moreover, the model does not include surface migration. It supposes that the gas particles, once they hit the wall, stay there fixed in place until they desorb again. But the particles can also travel alongside the wall surface where they need to overcome the periodic lattice potential of the wall material. Furthermore, depending on the angle at which a gas particle hits the wall, there is the chance that the gas particle penetrates the surface and gets irreversably stuck deeper inside the surface material. This effect would lead to a further prolongation of the filling time. Since the fibers have been exposed to atmosperic pressure conditions before evacuation (flushing with nitrogen), there should still be a certain amount of nitrogen particles sticking to the fiber walls, when the rubidium is propagating to the insides of the fibers. Thus, rubidium atoms will be taken out of the system by chemical reactions. There is also a limitation of modeling the fiber filling dynamics using the diffusion equation. The diffusion equation only describes the dynamics of equalizing the particle density in space. It assumes that the particle density inside the fiber is tending to reach the outer particle density. The vacuum chamber and therefore also the chamber walls are filling much quicker with rubidium as the fibers will. Thus, a rubidium milieu is established much more quickly inside the chamber than inside the fibers. The vapour pressure for any substance at a given temperature is defined as the pressure value established in a thermodynamical equilibrium of the substances phases in a closed system. So, once a rubidium milieu has build up, the rubidium gas pressure will be simply the vapour pressure. Inside the fibers, the situation is different. For the diffusion process, the fiber walls have been taken to be nearly unoccupied with rubidium particles. The gas pressure inside the fibers will thus not arise from an equilibrium of interacting rubidium atoms (the mean free path is many orders of magnitude larger than the fiber core's radial dimensions), but from an equilibrium of atom-surface interaction.
It is difficult to estimate on how much these effects modify the diffusion coefficient and it is imaginable that the caused shift lies within the order of the absolute value of the diffusion coefficient. At last, there is to mention that Langmuirian adsorption has been neglected which reduces the filling time. On the one hand, there is on overestimation of the filling time due to the neglection of wall occupation and on the other hand, there is an underestimation as the exponential prefactor has been taken to be at the lower limit of its range in the order of $10^{-13}$ seconds. As a result, the calculated filling times are regarded only as an indicator of the order of magnitude of the actual time the diffusion process takes. Knowing the conditions inside one fiber allows for a conclusion of the conditions inside the other fibers, as only the absolute time scaling

is not exactly known, whereas the relative scaling between the fibers stays mostly unaffected by this lack of knowledge. The filling time is proportional to $\frac{1}{r^2}$ where $r$ is the fiber core radius. This reveals a very strong dependence of the diffusion process on the transversal dimensions of the fibers.
To unfold the diffusion dynamics of a given system has turned out to be extremely difficult. Even in literature, there are applied different approaches to this kind of problem [33,34,35,27,28]. Unfortunately, no freely available source has been found that presents a theoretical diffusion model coinciding well with experimental data for the conditions given here.

## 4.5. Experimental observations on the rubidium diffusion process into the fibers

After the vacuum system has been arranged, it was unclear, how long it would take for rubidium to diffuse into the fibers. The time scale has been observed to range from hours to month before by others.
The first fiber the laser beam has been coupled into was the PDMS H8003 fiber. This fiber type has the largest radius compared to the others and should therefore fill with rubidium quickest. The filling should therefore advance such that the change in absorption depths for a laser beam passing through the fiber would be clearly visible in a matter of at least a few days. The coupling has been performed a few days after the rubidium release by ampoule breaking inside the vacuum chamber. Unfortunately, the diffusion process has by then not only been completed inside the chamber but also inside the fiber. Thus, the time period of significant change in absorption depth of the beam power signal has been missed. This observation is at least useful in a way that there is no need to wait much longer to perform measurements inside the fibers, since steady state conditions have already been established. And as the fiber radii do not vary by much, also the fiber with smallest radius should not take much longer to fill with rubidium than the PDMS H8003 fiber which was thought by the time these measurements where done.
The lack of data for the time period where the absorption signal depths changed significantly prevents from fitting the data to the calculations carried out within this chapter. This would have been very useful to overcome the problems raised by the unknown mean adsorption time of rubidium atoms on the wall surfaces and determine the diffusion dynamics in at least one fiber.
Thus, the obtained calculations underlie the restriction of not being varified by the experiment. It has been discovered, however, that the diffusion dynamics are highly dependent on the adsorption processes on the wall surface for being deep inside the molecular flow regime. The surface interaction can be responsible for a variation of filling times over orders of magnitude. Furthermore, the progress of atoms propagating to the inner fiber domain is dependent on the square of the radius of the fiber. Consequently, reducing the fiber radius by far leads to a remarkable prolongation of the filling time of fibers by atoms. These results explain why the diffusion dymanics

can take even month to complete rather than hours or days.

# 5. Light matter interaction for the rubidium $D_2$-transition line system

In this chapter, a closer look at the light-matter interaction for the rubidium $D_2$-transition line system is taken with the final goal of determining the rubidium pressure inside three different gas host structures: a pyrex glass cell, the vacuum chamber and most importantly the hollow core fibers.
At first, some physical and optical properties of rubidium are presented that are taken to be relevant later on. In connection, a theoretical model is presented [36] that has been developed and proven well experimentally for predicting the rubidium absorption behaviour in the low intensity limit where the absorption becomes intensity independent. In [36], an empirical parametrisation for the absorption behaviour at higher intensities is put forward. These results are then applied to the different gas host structures available here. For the pyrex glass cell and the vacuum chamber, the low intensity limit is reached. The parametrisation from [36] is fitted to the intensity dependent absorption signal and the gas particle pressures are determined. In the case of the fibers, the determination of the particle pressures is more complicated. On the one hand, the absorption contribution of the light directly before and behind the fibers that is already propagating inside the chamber has to be subtracted, as the fibers are not as long as the chamber. On the other hand, the low intensity limit is not reached for the light guided through the fibers due to the strong light confinement for all of the fibers. Therefore, there needs to be done an extrapolation to the low intensity limit using the parametrisation from [36]. Absorption measurements have been done for five different fibers. The obtained results for the gas particle pressures inside these fibers are then finally compared to those of the other gas hosts. Also the coupling efficiencies for the five fibers are presented.
For both used physical constants and presented rubidium properties in the following sections, [37,38] is consulted.

## 5.1. Specific rubidium properties

Hereinafter, some specific physical and optical rubidium properties are presented that are essential for its light absorption behaviour.
Rubidium atoms consist of 37 electrons and protons. Natural rubidium consists of two isotopes, $^{85}$Rb and $^{87}$Rb with abundances of 72.17(2) and 27.83(2) per cent and atomic masses of $m \approx 85.912u$ and $m \approx 86.909u$. Of these two isotopes only $^{85}$Rb is stable, whereas $^{87}$Rb tends to decay. But as it is only very weakly unstable and therefore has a long nuclear lifetime (nuclear lifetime $\tau_n = 4.88 \cdot 10^{10} years$), it can

be treated as being stable, too. The melting point of rubidium for both isotopes is $39°C$, the boiling point $688°C$. As a consequence, rubidium is found to be solid and has a very low vapour pressure at room temperature. At $T = 20°C$ (corresponds to $T = 293.15K$), the vapour pressure turns out to be $p_{vap} = (2.1 \pm 0.1)10^{-7} torr$. This value is obtained by consulting the vapour pressure curves shown in A.1 and A.2 in the appendix. The curves are slightly different for the two isotopes. Thus, the vapour pressure values at $20°C$ read off the curves[1] are weighted according to their natural abundances to yield this total pressure value. The partial vapour pressures of the isotopes are $p_{partial} = 0.7217 \cdot (2.2 \pm 0.1)10^{-7} torr$ for $^{85}$Rb and $p_{partial} = 0.2783 \cdot (1.9 \pm 0.1)10^{-7} torr$ for $^{87}$Rb.
Rubidium is an alkali metal. It has thus one electron in its outermost shell which results in a hydrogen-like energy spectrum. Here, only the rubidium $D_2$-lines are of interest. These lines correspond to the transitions $5^2S_{\frac{1}{2}} \leftrightarrow 5^2P_{\frac{3}{2}}$. This transition system can be accessed by an outer light source with a wavelength of $780nm$. The $D_2$-hyperfine splittings of the two isotopes are shown in the figuresA.3 and A.4 in the appendix. The differences in the splittings for the isotopes arise out of the isotope mass shift on the one hand and the different nuclear spins on the other hand. $^{85}$Rb has a nuclear spin of $I = \frac{5}{2}$, whereas the nuclear spin of $^{87}$Rb is $I = \frac{3}{2}$. For both isotopes, the ground state $5^2S_{\frac{1}{2}}$ is split into two branches and the excited state $5^2P_{\frac{3}{2}}$ into four branches of different total angular momentum $F$ where each of these states is further degenerate by the multiplicity $2F + 1$ into the single eigenstates. Rubidium atoms in the ground state will be consequently found in a superposition of the two ground state levels that depends on temperature. The temperature induced weight factor for a ground eigenstate is a Boltzmann factor.
If a ground state rubidium atom is located inside an outer photon field, transitions to excited states are possible by photon absorption. Since the rubidium wave function is concentrated to a very small area in space compared to the dimension of the wavelength resonant with the $D_2$-lines, the atom-light coupling is governed mainly by a dipole contribution. As a photon couples two different rubidium atom eigenstates, the dipole matrix element for these two eigenstates needs to be calculated. It yields the individual coupling strength of the transition. A vanishing dipole matrix element indicates that a transition will not occur or is strongly surpressed. The individual strength factors $C_F^2$ for the $D_2$-lines are shown in table A.5 in the appendix. In each of these factors, the individual Zeeman level contributions have already been summed up. The table shows that for both isotopes each ground level with a given total momentum $F$ can be excited to three different states distinguishing in the new total momentum $F\prime$. As a result, there are a total of twelve possible transitions in the $D_2$-line system of both isotopes. The decay rate $\Gamma$ and the lifetime $\tau$ are equal within the error ranges for all of the excited states and the two isotopes in the $D_2$-line system. They are given by:

[1] There are also given parametrisations of the vapour pressure curves in [36,37], but both approaches yield the same values and errors for the particle pressures.

$^{85}$Rb: $\Gamma = 38.117(11)10^6 s^{-1}$, $\tau = 26.2348(77) ns$
$^{87}$Rb: $\Gamma = 38.11(6)10^6 s^{-1}$, $\tau = 26.24(4) ns$

## 5.2. Presentation of a light-matter interaction model for rubidium

In this section, the light matter interaction model from [36] for rubidium atoms will be presented shortly and the different influences contributing to the overall absorption coefficient will be explained. [36] focusses on analysing the absorption behaviour of both the rubidium $D_1$- and $D_2$-transition line systems. For a more detailed look, [36] can be consulted.
For monochromatic light propagating along the $z$-axis through a uniform density atomic vapour, the absorption is described by the Beer-Lambert-law:

$$I(z) = I_0 e^{-\alpha(\nu,T)z} \tag{5.1}$$

where $I(z)$ is the intensity at position $z$ within the atomic vapour, $I_0 = I(z = 0)$ is the intensity of the incoming light, $\nu$ is its frequency, $T$ the temperature of the vapour and $\alpha$ the so called absorption coefficient. The latter contains all effects that contribute to light absorption.
The transmission $\mathcal{T}$ of the incoming light through a gas container which provides an overall interaction length of $L$ is then given by

$$\mathcal{T} = \frac{I(z = L)}{I_0} = e^{-\alpha L}. \tag{5.2}$$

Note that the absorption coefficient is assumed to be intensity independent here. This is only true, if the intensity is very weak.
The intensity dependence of the transmission can be easily made plausible. For a very low intensity beam of light entering an atomic vapour filled gas host with a frequency close to an atomic transition, the gas atoms are all found to be in their ground state inside the outer photon field and interact with this field according to a certain probability. As the beam intensity rises, hyperfine pumping becomes relevant. More and more atoms will be in an excited state an thus unable to absorb a photon. For a high intensity beam, there is a saturation level where all atoms are found to be approximately half of the time in an excited and the ground state. It is apparent that this saturation levels is determined by the lifetime of the excited state. By further increasing the beam intensity, the fraction of photons absorbable by atoms decreases with the light transmission approaching 100 per cent. Therefore, the transmission will first of all be on a constant plateau for low beam intensities and tends to asymptotically approach the 100 per cent value for ever growing beam intensity. A more quantitative analysis of how high the intensity needs to be to leave the low intensity plateau for the transmission will be given later on.
In general, a medium consists not only of one but of several species, each with multiple

transitions. Consequently, the transmission will be modified in the following way, just summing up the individual contributions $\alpha_i$ of the individual absorption coefficients:

$$\mathcal{T} = e^{\sum_i \alpha_i L}. \tag{5.3}$$

For a rubidium atomic vapour, there are two species, namely the two isotopes $^{85}$Rb and $^{87}$Rb. Overall, these two species incorporate twelve possible atomic transitions as discussed in the previous section. Each of these transitions (that links a ground state level $F_g$ to a certain excited level $F_e$) has an absorption coefficient of the following form for the detuning $\Delta = \omega_L - \omega_0$ ($\omega_L$: angular laser frequency, $\omega_0$: angular frequency of the transition):

$$\alpha_{F_g F_e} = k C_F^2 d^2 n \frac{1}{2(2I+1)} \frac{1}{\hbar \epsilon_0} s(\Delta). \tag{5.4}$$

The single contributions for such an $\alpha_{F_g F_e}$ are given as follows. $k$ is the wave vector of the incoming laser light. $C_F^2 d^2$ represents the dipole matrix element calculation. $C_F^2$ are the individual line strength factors introduced in the last section and $d$ is a proportionality factor which is given by $d = 5.177 \cdot e a_0$ ($e$: elementary charge, $a_0$: Bohr radius) for the rubidium $D_2$-lines. $n$ is the particle density which is, according to the ideal gas law, given by $n = \frac{p_{partial}}{k_B T}$ ($k_B$: Boltzmann constant, $T$: temperature) where $p_{partial}$ corresponds to the partial pressure of either $^{85}$Rb or $^{87}$Rb. $2(2I+1)$ with nuclear spin $I$ is the degeneracy of the ground state of the particular isotope (12 for $^{85}$Rb and 8 for $^{87}$Rb). At room temperature, the Boltzmann factor for the two different $F_g$ hyperfine states of each isotope is unsignificantly smaller than 1 which results in an evenly distributed population amongst the ground state Zeeman sublevels. On the other hand, the Boltzmann factor decreases fast enough for higher energy differences such that the population of excited levels is reduced to a negligible level. $\hbar$ is the reduced Planck constant and $\epsilon_0$ the electric field constant. $s(\Delta)$ describes the transition line broadening due to the Doppler effect. It is a voigt profile resulting out of a convolution integral of the natural Lorentz profile of the transition and the Gaussian velocity distribution of the rubidium gas atoms:

$$s(\Delta) = \int_{-\infty}^{\infty} f_\Gamma(\Delta - kv) \cdot G(v)\, \mathrm{d}v \tag{5.5}$$

with

$$G(v) = \frac{1}{\sqrt{\pi u^2}} e^{-\frac{v^2}{u^2}} \tag{5.6}$$

and

$$f_\Gamma(\Delta - kv) = \frac{\frac{\Gamma}{2}}{(\frac{\Gamma}{2})^2 + (\Delta - kv)^2} \tag{5.7}$$

($v$: velocity, $u = \sqrt{\frac{2k_B T}{m}}$, $m$: rubidium isotope mass).

The laser is assumed to be a monochromatic wave, since its bandwidth of $2 - 3MHz$ is negligible compared to the Doppler broadening. This does not hold for

the unbroadened Lorentz profile, however. According to $f_\Gamma(\Delta - kv)|_{v=0}$, the FWHM value for the Lorentz profile is given by

$$FWHM = \frac{\Gamma}{4\pi} \approx 3.0MHz \tag{5.8}$$

which is just as broad as the laser bandwidth. Since the vapour pressure of rubidium is very low at room temperature, the effect of gas atom collisions on the transition lines within the laser beam does not play a role. At last, the expected transmission profile for the light-matter interaction can be calculated as a function of detuning.

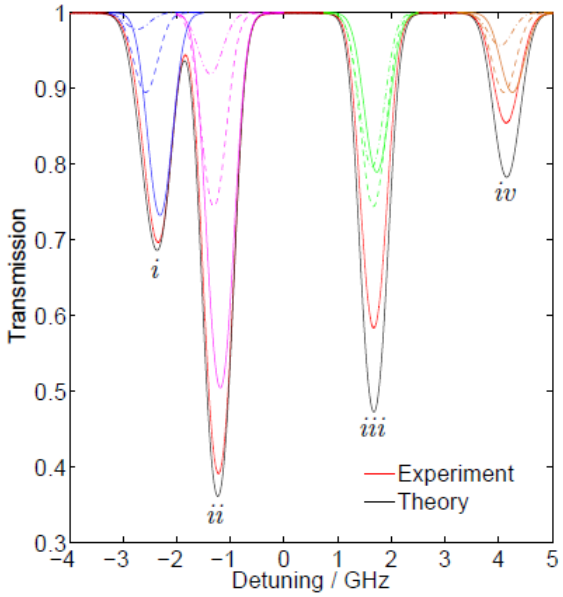


Figure 5.1.: Transmission through a vapour cell with a length of $7.5cm$ at $25.4°C$ and a beam width of $(2.00 \pm 0.05)mm$, for the rubidium $D_2$-line system. The solid black line represents the absorption signal predicted by theory. Superimposed are the expected transmissions for the individual hyperfine transitions. In the low intensity limit, the experimental result would overlap with the theoretical prediction with respect to the curve linewidth. The solid red line is the experimentally measured transmission for an intensity exceeding the low intensity limit and thus showing the role of hyperfine pumping in absorption spectroscopy on the $D_2$-line-system. Taken from [36].

In figure 5.1, the absorption signals for sweeping over the rubidium $D_2$-transition lines at $25.4°C$ for a rubidium vapour filled cell of a length of $7.5cm$ and a beam width of $(2.00 \pm 0.05)mm$ are shown. The black curve represents the theoretical calculations. The transmission profiles for the individual twelve hyperfine transitions are

also included. They are represented by the differently coloured, dotted lines plus the strongest, solid line. The redly coloured curve is explained later on. The experimental data for the low intensity limit would be found to overlap completely with the theoretical prediction as a consequence of the linewidth of the curves which is bigger than the deviation between theory and experiment. There are four main absorption dips observable. The dip corresponding to the $F_g = 3$ ground state transitions of $^{85}$Rb is found to be deepest. The further ordering in line center transmission depth is given as follows. The second deepest dip corresponds to the $F_g = 2$ ground state transitions of $^{85}$Rb followed by the $F_g = 2$ ground state transitions of $^{87}$Rb and ultimately those corresponding to the $F_g = 1$ transitions of $^{87}$Rb. It is quite remarkable that the line center absorption depths at room temperature for interaction lengths of roughly $10cm$ are neither close to 0 nor to 100 per cent transmission, although the absorption is highly sensitive on the interaction length and gas vapour pressure. This makes the verification of the theoretical predictions by measurements quite convenient.
The introduced formulas only hold for the low intensity limit where hyperfine pumping effects can be neglected. The reference value for beam intensity strength for a specific atomic sample is determined by the atom transition lifetime $\tau$ and the wavelength *lambda* of the incoming laser light. It is given by the so called saturation intensity

$$I_{sat} = \frac{\pi hc}{3\lambda^3 \tau}. \tag{5.9}$$

For the rubidium $D_2$-line system, the saturation intensity turns out to be $I_{sat} = (16.7 \pm 0.1)\frac{W}{m^2}$.
In [36], the weak intensity limit for a laser beam of a width of roughly $2mm$ is found to be reached at more or less $\frac{I}{I_{sat}} \approx 0.001$ where further decreasing of the intensity does not change the absorption anymore within the error range. $I$ is the peak intensity value for the Gaussian laser mode.
There is found excellent agreement between the theoretical model and experimental data ranging from a transmission of $5 - 95$ per cent for a gas host length of $7.5cm$ at room temperature ($25°C$). The rms discrepancy is in the order of 0.2 per cent where the measured absorption is slightly smaller than the predicted value. This is taken to be probably the consequence of the broad pedestal of the emission from the laser and also the finite laser linewidth which was in the order of 0.1 per cent of the Doppler width.

Furthermore, [36] outlines the consequences of hyperfine pumping effects on the absorption signal for beam intensities exceeding the low intensity limit. The reduction of the absorption depth is of different extent for the four main absorption dips observable at room temperature which is shown by the red absorption line in figure 5.1. In order to visualize the pumping effects more elegantly, there has been done a plot of the ratio $\frac{\alpha(I)}{\alpha(0)}$ for the central line absorption depths in dependence of $\frac{I}{I_{sat}}$ for several of the main dips of the $D_1$- and $D_2$-transition lines which is shown in figure 5.2. The theoretical prediction for a Doppler broadened medium consisting of two level atoms of the form

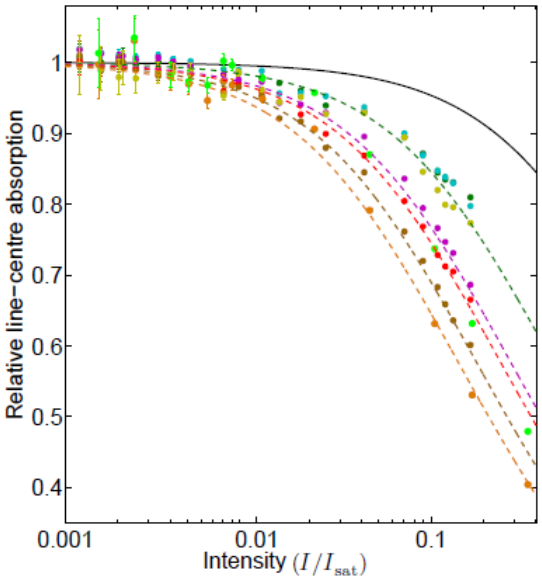


Figure 5.2.: Normalized line-center absorption showing the effects of hyperfine pumping for main absorption dips of both the $D_1$- and $D_2$-transition line systems of rubidium. The solid line is the theoretical prediction for a Doppler-broadened medium of two-level atoms. The dotted lines are guides to the eye. Taken from [36].

$\frac{1}{\sqrt{1+(\frac{I}{I_{sat}})}}$ is also included. The data points are fitted to curves of the form $\frac{1}{\sqrt{1+b(\frac{I}{I_{sat}})}}$ with $b$ being a parameter that is said to characterize the effective reduction in saturation intensity. It should be noted that $I$ represents the peak value for the intensity of a Gaussian mode. The transversal intensity distribution is not considered here, but it should be in a rigorous theoretical derivation for the decrease of the line center absorption with increasing laser beam intensity. However, the variation of intensity in transversal direction for the Gaussian beam is irrelevant as long as hyperfine pumping does not play a role. The parametrisation just presented has been used as a "guide to the eye", but it seems to describe the actual data quite well. It should be applicable well for the conditions of this experiment, since the relevant parameters are similar. Nevertheless, it should be kept in mind that this parametrisation is just empirical.

## 5.3. Application of the theoretical model on different gas hosts

After the theoretical model of light-matter interaction for the rubidium $D_2$-line system has been introduced, it can be applied to the rubidium vapour filled hosts available here. The data of the line center absorption depths for the deepest absorption line

(transitions for$^{85}$Rb from the ground state $F_g = 3$) is extracted from the absorption signals of a laser beam transmitting the pyrex glass cell, the vacuum chamber and five different fibers inside the chamber. This is done for different laser beam intensities ranging over several orders of magnitude - from the lowest beam powers measurable by the photodiodes to the order of maximal beam powers realisable for the $80mW$ laser for (rather) constant beam radii. The intensity dependent line center absorption depth is plotted over the ratio $\frac{I}{I_{sat}}$ and fitted using the parametrisation presented at the end of the previous section. The maximal line center absorption depth is reached for vanishing beam intensity. This maximum value is taken from the fit and inserted in the theoretical model of light-matter interaction (where hyperfine pumping effects play no role) to determine the rubidium gas pressures in the different gas hosts, once steady state conditions have been reached.

Before the data are taken, there is tried to get an estimate of the error of the beam power measurements by the power sensor. It has been tested, how the beam power measurements are influenced by beam size variation, by absorption position variation on the detection surface and by exchange of the beam power sensor. The influence of beam size variation has been tested by inserting the power sensor into the beam path behind a focussing lens of the optics setup. The absorption position influence has been analysed at a position where the beam size was very small compared to the sensors detection area. The different power values for the laser beam falling onto the central part, the upper, lower, leftmost and rightmost edges of the detection area have been recorded. Additionally, there have been used two more power sensors to get an idea of the error of sensor calibration. Therefore, the beam power falling onto three different power sensors has been compared.
These measurements have been carried out at different beam powers ranging over several orders of magnitude. The trend of the beam power errors is in harmony with the expectation. For ever decreasing beam power, the uncertainty increases ever more. Once falling below a certain power value, also light of external light sources has an influence on the actual power measured by the sensors despite efforts of shielding the sensor surfaces from outer light sources.

After adding up the beam power errors arising due to different beam sizes, different absorption positions on the detection area and different sensor calibrations, the percentage of the power error can be plotted in dependence of the absolute power. This is shown in figure 5.3. The data points have empirically been found to be well described by and thus fitted to a function of the form

$$y = \frac{a}{\sqrt{x}} + b\,. \tag{5.10}$$

This parametrisation makes sense, since it diverges for ever decreasing beam power and converges for ever increasing beam power to a constant minimal value for the percentage beam power error. The fit function can be used to inter-/extrapolate the

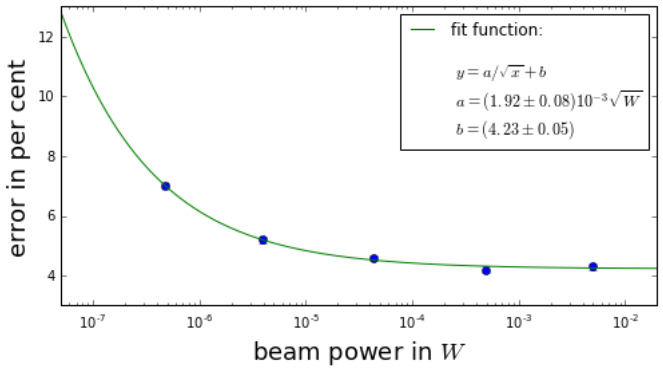


Figure 5.3.: Beam power error of the power sensor in per cent for different beam powers. The data points have been fitted to allow and inter-/extrapolation of the beam power error to any power value.

corresponding error to all beam powers measured later on. The error range for beam powers ranges from $4-5$ per cent for the highest powers recorded ($\approx 10mW$) to $10-11$ per cent for the lowest powers recorded ($\approx 100nW$). This error is added up to the power fluctuations for every individual beam power measurement carried out. These flucutations are either originating from outer light sources, the diode laser or the triangular sweeping over the transitions which changes the current applied to the laser diode, respectively.
Another issue that has to be taken into account is the absorption/reflection properties of the entrance windows of the gas containers. Therefore, not the beam power measured directly in front of the containers represents the incoming beam power, but the fraction actually transmitting the entrance window. In order to determine this effect, the laser frequency has been detuned slightly out of the rubidium lines. This detuning is that small that the change in absorption/reflection for the windows due to their frequency dependence is negligible. The beam power has been changed in a range of several orders of magnitude and recorded in front of and behind both the vacuum chamber and the pyrex glass cell with the power sensor. The absorption/reflection has been found to be power independent. It was assumed that both entrance and exit windows have the same effect (and thus the same thickness) on the laser beam with respect to power decrease. For the pyrex glass cell, the beam power after passing through one windows is reduced to $(92 \pm 1)$ per cent of its initial value. For the vacuum chamber, a reduction to $(91 \pm 2)$ per cent of the initial value has been observed. Thus, both the vacuum chamber and pyrex glass cell windows have basically the same impact on the beam power reduction.
In order to transform the beam power into corresponding intensity values, the beam radius has to be measured in front of and behind the different gas hosts which was done with the camera. Since the beam size changes along the beam's propagation axis for the Gaussian mode, the obtained values have been averaged for both horizontal

and vertical axis. The beam size error range is then mostly given by the values measured in front of and behind the gas containers. The relation between beam power $P$ and peak intensity $I$ for the Gaussian mode is given by

$$I = \frac{P}{\frac{w_x w_y}{2}} \,. \tag{5.11}$$

The total power $P$ is obtained by integrating the intensity distribution over the whole transversal plane. $w_x$ and $w_y$ are the beam radii for the horizontal (x) and vertical (y) axis. Therefore, an elliptic deshaping of a circular Gaussian mode has been considered here. Together with the saturation intensity $I_{sat} = (16.7 \pm 0.1)\frac{W}{m^2}$ for the rubidium $D_2$-line system, the ratio $\frac{I}{I_{sat}}$ can be calculated. As presented in the last section, the variation of the beam intensity in transversal direction is not further considered. This has not been done for the parametrisation from [36] for the intensity dependence of the absorption coefficient.
Next, the error contributions for the transmission signals need to be discussed. At first, the current for the laser diode has been set to a value corresponding to a frequency in the rubidium $D_2$line system. The triangular voltage signal from the frequency generator (which was used to sweep over the rubidium $D_2$-lines, changing the current linearly) and the oscilloscope time base have been chosen such that all four main rubidium absorption dips as well as the entire falling flank of the triangular voltage signal (to which the oscilloscope was triggered) could be seen on the oscilloscope screen. Afterwards, the absorption signals for vacuum chamber, pyrex glass cell and fibers along with the beam powers have been recorded. The beam power has always beam increased by a factor of 3 from data point to data point beginning with a beam power of roughly $100nW$. The data taking could be done by leaving the photodiode gain constant while changing the oscilloscope voltage range or leaving the oscilloscope's voltage range constant while changing the photodiode gain. For every gain level of the photodiode, there was a constant signal offset which had to be subtracted from the recorded absorption signals.
The absorption signals have afterwards been cutted at both ends of the falling triangular flank of the frequency generator signal and fitted to a function including four Gaussians plus a linear contribution. The linear contribution was included due to the triangular voltage signal of the function generator which results in a change of current and consequently in a change of power. The linearity in power change has been found to be a very good approximation for most of the signals. Of further interest is only the line center absorption depth for the $^{85}$Rb isotope corresponding to transitions from the ground state $F_g = 3$. Therefore, only the prefactor $A$ of the corresponding Gaussian is extracted from the absorption signal data.
The error of this prefactor comprises three contributions. Firstly, there is the signal noise. The signal to noise ratio rises for decreasing beam power, but has only been found to be of great impact for the data points taken for the lowest beam power ($\approx 100nW$). Secondly, the recording of the absorption depth is limited by the oscilloscope's resolution. For high beam powers (from roughly $1mW$ upwards), the absorption dips are very small and thus getting close to and even below the resolution

limit. This has been observed to be a problem mostly for the smaller absorption dips where the fit program was no longer able to identify all four main absorption dips anymore. Thirdly, the beam power variation as a consequence of the linear detuning by the function generator. This resulted in a periodical movement of the 100 per cent transmission level. This effect is most relevant for high absorption depths. The impact of these three error contributions has been estimated for all absorption depths and added up to form the total absorption depth error. The transmission is then obtained by subtracting the normalised prefactor (which is the ratio of $A$ and the corresponding voltage level for 100 per cent transmission) from the 100 transmission level (100 per cent corresponds to 1).
Up to now, the line center transmission and its error for the vacuum chamber and the pyrex glass cell have been discussed. This allows for fitting the data to the parametrisation presented in the last section and determining the line center transmission for vanishing intensity. As the fibers inside the vacuum chamber are not as long as the chamber, light is already absorbed before and behind the fiber's tips inside the chamber. The impact of this light absorption needs to calculated and added up to the line center transmission for the fiber data. Therefore, the fit for the vacuum chamber is needed.
Since the light is strongly focussing in front of and strongly defocussing behind the fiber tip, the beam radius can not be taken to be more or less constant anymore. This is treated as follows. The horizontal and vertical beam radii in front of the lens which itself is placed in front of the vacuum chamber have been found to be of nearly the same size. Therefore, the beam mode is treated to be circular for focussing. This is also taken to be true for the defocussing when the laser light leaves the fiber. Four of the five fibers considered in these measurements have been placed quite central inside the chamber. This means that there was roughly a distance of $0.5cm$ between each fiber tip to the entrance/exit window. For one fiber however, one tip was located directly at the exit window. Consequently, there was roughly a distance of $1.0cm$ between the other fiber tip and the entrance window. These distances are denoted by $d$ in the following calculations. According to the parametrisation chosen for modeling the line center transmission and including the beam radius change, the transmission $\mathcal{T}$ of the laser light for an interaction length $d$ is given by

$$\mathcal{T} = e^{-\int_0^d \frac{az}{\sqrt{1+b(\frac{I(z)}{I_{sat}})}}\mathrm{d}z} \tag{5.12}$$

with the parametrisation fit parameters $a$ and $b$. It can be seen that $a$ represents the absorption coefficient for vanishing intensity $I$. Here, the fit parameters calculated for the line center transmission of the absorption signals for the vacuum chamber data have to be inserted. For a circular beam, $I$ is linked to the beam power $P$ by

$$I(z) = \frac{P}{\frac{w(z)^2}{2}} \tag{5.13}$$

where $w(z)$ is the beam radius.

The beam radius $w(z)$ is given by

$$w(z) = w_0\sqrt{1+(\frac{z}{z_0})^2}\,. \tag{5.14}$$

Two different values have to be inserted for the beam waist radius $w_0$ (and consequently for the rayleigh range $z_0$ as well) depending on whether the focussing or defocussing beam is considered. The beam waist radius $w_0$ for the laser beam before entering a fiber has been calculated already. It is determined by the $q$-parameter after the laser's transmission through the $100mm$ lens which is placed in front of the chamber. Its value has been calculated to be $w_0 = (38.9 \pm 0.5)\mu m$ in chapter 3.2. The beam waist radius at the fiber tip where the laser exits the fiber is given by the fiber's mode field radius. It is thus different for every one of the fibers. The mode field radius of the fibers used in this experiment is said to be given by multiplying the inner core radius (shown in figure 3.6) with $\frac{\pi}{4}$ (private communications with [20]).
Once the transmission $\mathcal{T}$ has been calculated, the corresponding absorption $1-\mathcal{T}$ needs to be finally added up to the line center transmission depths for the fiber data. Both the contribution for the focussing and the defocussing need to be considered here and have been added up. The absorption value has been found to be roughly 3 per cent for the data point with lowest beam power for every fiber. It decreased more or less linearly with each subsequent data point. The errors for the just presented procedure also need to be taken into account. Since the lens is not placed exactly $100mm$ before a fiber tip, the beam radius at the fiber tip will not be $w_0$ but rather a little bit larger. Similarly, all other parameters relevant for calculating $\mathcal{T}$ entail their own uncertainties. The overall contribution of all these uncertainties has been found to be less than 1 per cent for the first data point decreasing further for subsequent data points.
Ultimately, the data for the absorption behaviour inside the fibers is determined and can be fitted to the parametrisation as well.
For all of the gas hosts, the transmission takes the following form:

$$\mathcal{T} = e^{-\frac{al}{\sqrt{1+b(\frac{I}{I_{sat}})}}} \tag{5.15}$$

with the fit parameters $a$ and $b$ and the interaction length $l$. There can now be introduced the decomposition $a = a\prime p_{^{85}Rb}$. $p_{^{85}Rb}$ represents the partial pressure of the $^{85}$Rb isotope. At room temperature ($20°C$), the isotopes vapour pressure is given by $p_{^{85}Rb} = 0.7217(2)\cdot(2.2\pm0.1)10^{-7}torr = (1.59\pm0.08)10^{-7}torr$. For the zero intensity limit, the transmission simplifies to

$$\mathcal{T} \to T_0 = e^{-al} = e^{-a\prime p_{^{85}Rb}l} \tag{5.16}$$

where $T_0$ is the line center transmission for vanishing beam intensity. Since the absorption coefficient $a$ at the line center transmission of the $^{85}$Rb isotope for the transmissions corresponding to the ground state $F_g = 3$ is known, as it can be calculated by the theoretical model presented in the last chapter, $a\prime$ can be calculated. It is given by

$a\prime = (6.21 \pm 0.03)10^7 \frac{1}{m \cdot torr}$. Thus, the partial $^{85}$Rb pressures can finally be calculated as well applying an equivalence transformation:

$$p_{^{85}Rb} = \frac{ln(\frac{1}{T_0})}{a\prime l} \,. \tag{5.17}$$

The ratio between the rubidium vapour pressure and the rubidium pressures inside the gas containers can then be obtained by the ratio of the partial pressure of the $^{85}$Rb isotope and the partial pressure of this isotope determined inside the gas containers.

### 5.3.1. Results for the pyrex glass cell and the vacuum chamber

Before the results are presented, the expectations are recapitulated shortly.
For an ever decreasing light intensity, the line center transmission depth for light matter interaction for a transition line rises, deviating more and more from the asymptotic limit of 100 per cent transmission for an infinite intensity. Once the intensity draws close to the saturation intensity characteristic for a transition, the line center transmission curve gets to a turning point where its derivative is maximal. For intensities much smaller than the saturation intensity, the line center transmission depth converges to its maximum value in the low intensity limit.
Applying the theoretical model for the line center transmission for the low intensity limit to the vacuum chamber and pyrex glass cell and assuming the rubidium pressure to be the vapour pressure at $20°C$, the transmission profile shown in figure 5.4 for the entire $D_2$-transition line system is obtained.

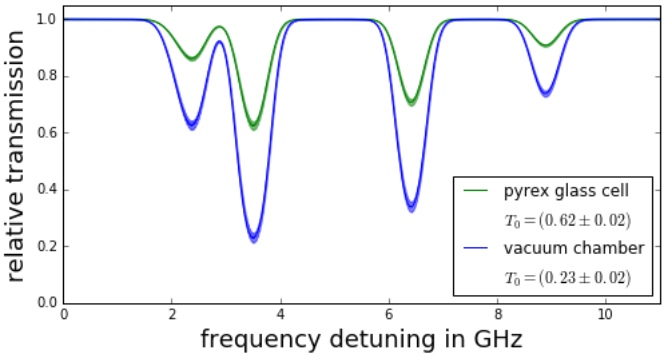


Figure 5.4.: Transmission profile of the rubidium $D_2$-transition line system in the low intensity limit. The profiles predicted for the vacuum chamber and the pyrex glass cell together with the line center transmission depth of the $^{85}$Rb isotope corresponding to the transitions of the ground state $F_g = 3$ are shown. The linewidth represents the uncertainty at room temperature ($20°C$) conditions for the rubidium vapour pressure.

Therein, the experimentally obtained transition frequencies of the figures A.3 and A.4 have been used. The linewidth represents the uncertainty at room temperature

($20°C$) conditions for the rubidium vapour pressure and consequently the error for the line center transmission depth $T_0$ for both vacuum chamber and pyrex glass cell which is shown in the legend.

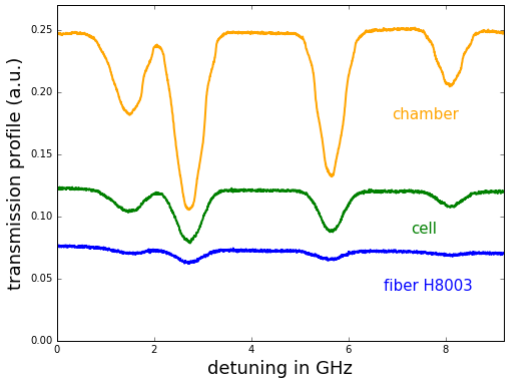


Figure 5.5.: Transmission profiles for a beam passing through the vacuum chamber, pyrex glass cell and PDMS H8003 fiber. The profiles have been recorded at beam intensities where the line center depths have been found to be deepest. The signals have been calibrated to the theoretical signal shapes shown in figure 5.4.

The actually measured absorption signals are plotted in figure 5.5. The transmission profiles for the beam passing through the chamber, the cell and the PDMS H8003 fiber are shown at beam powers where the line center depths have been found to be deepest. The signals have been calibrated to the theoretical transmission profile of 5.4. The widths of the absorption dips have been observed to be almost identical for all three gas hosts when four Gaussians (plus a linear background) are fitted to the profiles. The proportions of the different line center depths are coinciding with the theoretical prediction. Such absorption signals have been recorded and used for the plots presented in the following.
The measured intensity dependent line center transmission depths together with the limit value $T_0$ are shown in figure 5.7 for the vacuum chamber and in figure 5.6 for the pyrex glass cell. $T_0$ can be calculated with the curve parametrisation and the absorption coefficient $a$ for vanishing beam intensity. The calculated value is shown in the legend.

At first, the blue coloured data has been obtained by a measurement for the pyrex glass cell and the vacuum chamber. Therein, for the first half and the second half of the taken data points, the photodiode gain has been kept constant, while the voltage range of the oscilloscope has been changed. This corresponds to the attribute range changed. For the pyrex glass cell, the line center transmission is in harmony with the expectation within the error range. This is not the case for the data belonging to

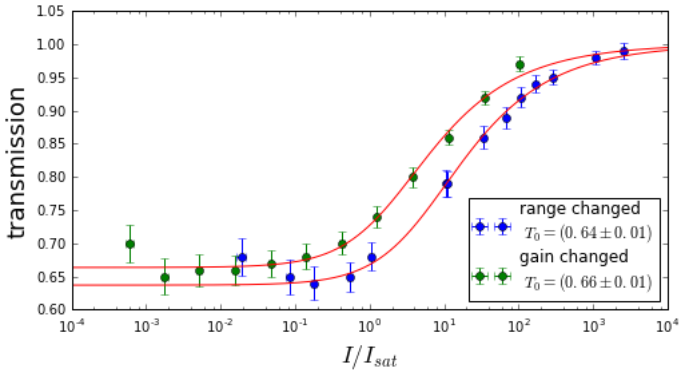


Figure 5.6.: Intensity dependence of the line center transmission depth for the pyrex glass cell. The blue coloured data has been measured for mostly constant photodiode gain while the voltage range of the oscilloscope has been kept constant (range changed). For the green coloured data, this has been handled vice versa (gain changed). Both data sets have been fitted to the parametrisation presented in 5.2. The line center transmission depths $T_0$ for vanishing beam intensity are shown in the legend.

the vacuum chamber. The line center transmission depth has been found to decrease again at low beam intensities instead of converging to a maximum in depth. As this could not be explained by any error contributions considered so far and also occured for changing the photodiode, it was suspected that this behaviour was a consequence of the electronics fabricated into the oscilloscope or the photodiodes.
Therefore, there has been done another measurement for both the vacuum chamber and pyrex glass cell. This time, the gain has been changed, while the oscilloscope voltage range has been kept constant. The oscilloscope range has only been changed for high intensities, as there are only eight different gain levels available for the photodiodes. This corresponds to the attribute gain changed and the green coloured data points. For the pyrex glass cell, the beam size has been increased by roughly a factor of ten for both horizontal and vertical direction additionally. The decrease in line center transmission has still been observed for the vacuum chamber data. But surprisingly, the line center transmission depth is not as large as before anymore for both vacuum chamber and pyrex glass cell. For some data points, the deviation is not within the error ranges. This shows the effect different electronic settings exert on the data. It should be noted as well that the time period lying between these measurements (blue and green coloured data) has been about a week and consequently also long time fluctuations for the conditions inside the gas hosts could play a role. But this is ruled out, as the temperature and thus the rubidium pressure did not fluctuate significantly during the time period within which the measurements have been performed. Nevertheless, the decrease in line center transmission for the vacuum chamber still remains unexplained. It can be seen that above all the data

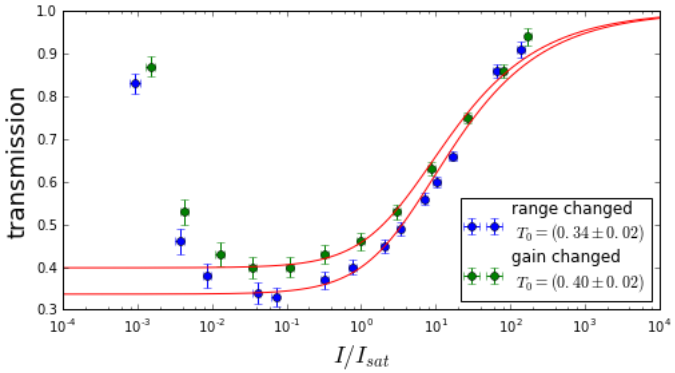


Figure 5.7.: Intensity dependence of the line center transmission depth for the vacuum chamber. The blue coloured data has been measured for mostly constant photodiode gain while the voltage range of the oscilloscope has been kept constant (range changed). For the green coloured data, this has been handled vice versa (gain changed). Both data sets have been fitted to the parametrisation presented in 5.2. The line center transmission depths $T_0$ for vanishing beam intensity are shown in the legend.

points for the lowest beam intensity show a large decrease in line center transmission. For these data points, however, with the photodiodes set to maximal gain, the beam power was at the lower edge of what the photodiodes are actually able to detect. Therefore, the offset voltage was bigger than the difference between the offset and 100 per cent transmission level. Consequently, it is assumed that the decrease in line center transmission results out of the lack of the detector to yield reasonable signals at the lower edge of its power detection range. This decrease has also been observed for the data obtained for the fibers which is presented in the next section.
For the fit of the data points to the parametrisation, the first three data points have not been considered for the vacuum chamber where the decrease in line center transmission depth plays a role. The parametrisation seems to describe the data quite well for the gas containers used here. Within the error range, the low intensity limit is reached here at roughly $\frac{I}{I_{sat}} \approx 10^{-1}$. This can be seen best for the green coloured data of the pyrex glass cell where the beam size has been broadened remarkably. This made it possible to reduce the beam intensity by two orders of magnitude compared to the blue coloured data. The reason why this limit is reached here for a larger ratio of $\frac{I}{I_{sat}}$ compared to the experiments performed in [36] can be explained by error sizes. The error sizes are much bigger here compared to those obtained in [36]. Furthermore it should be noted that not the ratio of absorption coefficients (figure 5.2) but the transmission has been plotted. The fit parameter $b$ that is said to characterize the effective reduction in saturation intensity has been calculated by the fit program to be in a range of $b = 0.25 - 0.65$.
The line center transmission values $T_0$ for the limit of vanishing beam intensity can

| container, data colour | pressure $p$ in $10^{-7}torr$ | ratio $\frac{p}{p_{vap}}$ |
|---|---|---|
| cell, blue | $(1.50 \pm 0.06)$ | $(0.94 \pm 0.07)$ |
| cell, green | $(1.39 \pm 0.06)$ | $(0.87 \pm 0.06)$ |
| chamber, blue | $(1.16 \pm 0.08)$ | $(0.73 \pm 0.07)$ |
| chamber, green | $(0.98 \pm 0.06)$ | $(0.62 \pm 0.06)$ |

Table 5.1.: Partial pressure values calculated for the $^{85}$Rb isotope together with the ratio of the obtained values and the partial vapour pressure $p_{vap} = (1.59 \pm 0.08)10^{-7}torr$ at room temperature ($20°C$) expected for the isotope. The calculations are based on the line center transmission depths for vanishing laser beam intensity obtained in the figures 5.6 and 5.7.

now be consulted to calculate the pressure inside both vacuum chamber and pyrex glass cell. It can be seen that both $T_0$ values obtained for the pyrex glass cell can be regarded as being equal within the error range. This is not the case anymore for the vacuum chamber where the deviation is larger. The corresponding pressures are calculated for all four $T_0$ values.

The results are shown in table 5.1. For a pure rubidium milieu, the pressure should coincide with the vapour pressure. Consequently, deviations from the vapour pressure give a hint that also surface interactions with other elements play a role and influence the transition into and out of the gaseous state.
For the pyrex glass cell, the calculated pressure for the blue coloured data coincides with the expected vapour pressure within the error range. The pressure value obtained by analysing the green coloured data, however, is found be a little bit smaller. The deviation of the two data sets has been traced back to arise from electronic components incorporated inside both oscilloscope and photodiodes. In this sense, both values obtained can be taken as coinciding with the expectation. This result confirms the pyrex glass to be a good choice as a container wall for rubidium vapour, as it does not modify the pressure to much by chemisorption and physisorption. Moreover, the cell has been fabricated several years before these measurements have been done. The amount of rubidium inserted has spread uniformly across the whole wall surface. It is assumed that the amount of rubidium inserted into such a cell is high enough to allow a layer of a thickness of many rubidium atoms to build up all along the wall. Thus, the transition into and out of the gaseous state is determined mainly by atom-atom binding forces of rubidium.
For the vacuum chamber, the same deviation between the two data sets occurs as observed for the pyrex glass cell. Neverthless, it can be seen that the calculated pressures are definitely smaller than the expected vapour pressure value. The obtained pressure values are roughly about 30 per cent smaller than the corresponding vapour pressure. This can be explained by a different wall material compared with the cell. The pyrex glass provides a dielectric interaction surface. Inside the vacuum chamber, the interaction surface is metallic. Therefore, the binding force of metal could be

larger and thus not allowing as much rubidium atoms to be in a gaseous state. This would result in a decrease of the rubidium gas pressure. The rubidium pressure has not been found to significanly change anymore a few days after the rubidium has been released into the chamber by breaking the ampoule as presented in 4.5. The measurements analysed in this chapter have been performed several weeks after the ampoule breaking. Therefore, a steady state condition should already have been built up for the dynamics on the chamber wall. This supports the conclusion drawn for the vacuum chamber.
Similarly, also the conditions inside the PDMS-coated H8003 hollow core fiber have been observed not to change anymore nearly a week after the ampoule breaking. Thus, a steady state condition should be reached inside the fibers as well which are next to be discussed.

### 5.3.2. Results for five different hollow core photonic crystal fibers

The expectation for the absorption behaviour inside the fibers is the same as for the pyrex glass cell and the vacuum chamber. The line center transmission depth should rise until finally reaching a maximum for vanishing laser beam intensity. For the fibers, the voltage range of the oscilloscope has been kept mostly constant while the photodiode gain has been changed. Therefore, the data for the fibers correspond to the green coloured data sets presented in the last section. For the transmission depth of the fibers, there has also been observed a decrease in line center transmission depth. This is, however, mostly restricted to the data point for the lowest been intensity which has not been considered for the fit of the data to the parametrisation presented in chapter 5.2.
The results obtained for the fibers are shown in figure 5.8. Ignoring the data point with lowest beam intensity for each fiber, the intensity dependence of the line center transmission depths is in harmony with the expectation. The parametrisation also seems to fit well for most of the data points within the error range.
In contrary to the observations made for both pyrex glass cell and vacuum chamber, there are two mayor differences for the line center transmission depths for the fibers. Firstly, the low intensity limit is reached for a larger value of the ratio $\frac{I}{I_{sat}}$ for all of the fibers. Even in a comparison between the different fibers, the low intensity limit is reached at a different ratio. The limit ranges from more or less $10^0 \frac{I}{I_{sat}}$ to $10^2 \frac{I}{I_{sat}}$. Thus, the low intensity limit was not needed to be extrapolated anymore for four of the five fibers, as it was already reached. Only for the PDMS-coated H2006 fiber, this has not been the case. The location of the low intensity limit at such high values of $\frac{I}{I_{sat}}$ manifests itself in a very low value of the fit parameter $b$ that is said to characterize the effective reduction in saturation intensity. It has values in the range of $b = 10^{-4} - 10^{-2}$. Secondly, the line center transmission depths for vanishing beam intensity and consequently the gas pressures are much smaller compared to the expected values determined by the vapour pressure at room temperature.
An explanation for the observation that hyperfine pumping effects get irrelevant at a much larger ratio $\frac{I}{I_{sat}}$ inside the fibers could be given by the following reasoning.

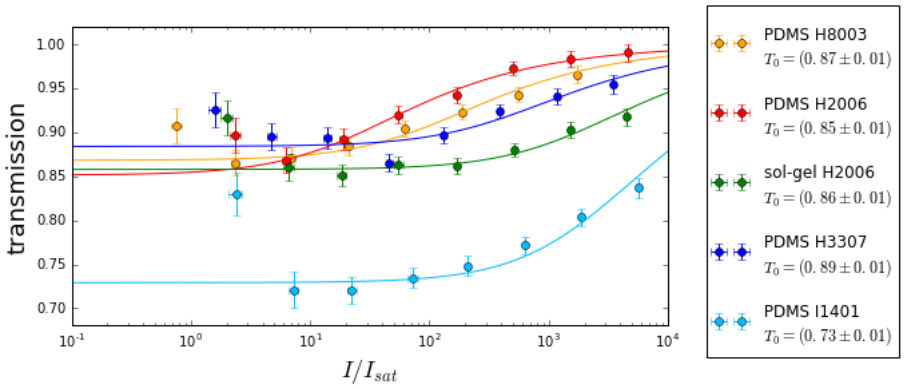


Figure 5.8.: Intensity dependence of the line center transmission depth for five different hollow core fibers. The data has been measured for mostly constant voltage range of the oscilloscope while the photodiode gain has been changed. The data sets have been fitted to the parametrisation presented in 5.2. The line center transmission depths $T_0$ for vanishing beam intensity as well as the fiber type are shown in the legend box.

In order to make hyperfine pumping effects relevant at a larger $\frac{I}{I_{sat}}$ value, somehow excited rubidium atoms need to be taken out of the beam path or be de-excited more quickly than predetermined by the lifetime of the excited state. The crucial difference between the systems discussed in the last section (vacuum chamber an pyrex glass cell) and the inner of a hollow core fiber is that inside a fiber wall collisins take place. Surface interaction is present inside a fiber in contrary to the situation in free space for the other two systems discussed. As the diffusion calculations in chapter 4 revealed, there should be much more rubidium atoms located on the wall surface than inside the hollow core volume. This is a consequence of the long adorption times compared to the time in between wall collisions for a Knudsen flow. Since the light intensity is concentrated at the core center, the interaction of light with the rubidium atoms should be most relevant for atoms moving in between the surrounding walls. Once such an atom is excited, it hits the wall, de-excites again and is replaced by another, ground state rubidium atom leaving the wall. Due to this process, more rubidium atoms seem to be found in the ground state compared to the situation outside the fibers (in free space, like in the vacuum chamber/pyrex glass cell) at a given light intensity peak value for the Gaussian mode. This effect would shorten the mean lifetime of an excited atom and therefore increase the associated saturation intensity. Another way of explaining the shift of the low intensity limit could be to argue that the four main absorption dips of the rubidium $D_2$-transition line system are significantly broadened in comparison with the absorption signals recorded for the vacuum chamber and the pyrex glass cell. This could then lead to a decreasing in the absorption depths. But this has not been observed to be the case in the signals

recorded which can be seen in figure 5.5. Wall interaction may lead to a shift or broadening of transition lines, but since the Doppler effect dominates the broadening of atomic transitions by far at room temperature, these effects remain unseen.
Unfortunately, there has not been enough time to record absorption signals for more than five fibers. In particular, no uncoated fiber is represented here. For the uncoated fibers, the wall interaction should be most intensive. The PDMS- and sol-gel-coatings are integrated inside such hollow core fibers in order to surpress surface effects unwanted in spectroscopy. The sol-gel-coated fiber data do not stand out compared to the PDMS-coated fibers here. Only the data for the PDMS I1401 fiber differ perceptibly from the other four fibers. Astonishingly, this fiber has the smallest core size of the five fibers but the largest rubidium pressure inside. Maybe for an ever decreasing radial extension of the fiber core, the difficulty of entering the fiber does not increase as fast as the difficultly of leaving it once a rubidium atoms has made its way inside. Since there is only this one fiber standing out in this regard, it is difficult to determine the reason for this behaviour. To get a clearer picture, a more extrem variation in fiber radii would have been needed. It is assumed that steady state conditions have been reached inside all of the fibers after several weeks of rubidium influx. This is due to the results obtained for the diffusion calculations and the observation of the absorption signals over one to two weeks after the ampoule breaking. The observation of quite small pressures is unexpected for the dielectric surfaces inside the fibers. For the pyrex glass cell, the pressure has been calculated to coincide quite well with the expected vapour pressure. The conditions inside the fibers obviously differs from the conditions inside the pyrex glass cell. A good explanation for this behaviour can not be given, as the exact impact of the interaction of rubidium with coatings like PDMS and sol-gel is unknown. This lack of knowlegde has already been found to restrict the predicting power of the presented diffusion model in chapter 4, since no reliable data for the mean adsorption times of rubidium on a PDMS- or sol-gel coated surface could be found. This was also problematic silica surfaces in the case of the uncoated fibers.

In table 5.2, the pressure values inside the five fibers and the ratio of these pressure values with respect to the expected value for the vapour pressure are shown. The pressures turn out to be more or less one order of magnitude smaller than the vapour pressure. Additionally, the coupling efficiencies for these fibers are displayed which are last to be discussed. They have been measured by detuning the laser frequency out of the $D_2$- transition lines and then recording the beam powers before and behind the chamber. The absorption/reflection properties of the chamber windows have already been determined in chapter 5.3. This additional effect in power decrease has been considered in the coupling calculations. The loss for the propagation of light through the fibers has been calculated in 3.3. For all of the fibers, the loss in beam power for light of a wavelength of $780nm$ is equal to or smaller than 1.6 per cent. The coupling has been performed by the $100mm$ lens which has been found to focus the beam radius down closest to the fiber's mode field radius. As a consequence of the strong light focussing and defocussing when the beam enters and exits the chamber, the light

| fiber type | pressure $p$ in $10^{-8}torr$ | ratio $\frac{p}{p_{vap}}$ | coupling efficiency in per cent |
|---|---|---|---|
| PDMS H8003 | $(1.60 \pm 0.15)$ | $(0.101 \pm 0.011)$ | $(69 \pm 3)$ |
| PDMS H2006 | $(1.87 \pm 0.16)$ | $(0.118 \pm 0.012)$ | $(99 \pm 4)$ |
| sol-gel H2006 | $(1.73 \pm 0.16)$ | $(0.109 \pm 0.012)$ | $(34 \pm 2)$ |
| PDMS H3307 | $(1.34 \pm 0.15)$ | $(0.084 \pm 0.011)$ | $(45 \pm 3)$ |
| PDMS I1401 | $(3.62 \pm 0.24)$ | $(0.228 \pm 0.020)$ | $(52 \pm 3)$ |

Table 5.2.: Partial pressure values calculated for the $^{85}$Rb isotope together with the ratio of the obtained values and the partial vapour pressure $p_{vap} = (1.59 \pm 0.08)10^{-7}torr$ at room temperature ($20°C$) expected for the isotope. The calculations are based on the line center transmission depths for vanishing laser beam intensity obtained in figure 5.8. Additionally, the coupling efficiencies for light transmitting the fibers is shown for the $100mm$ lens which is placed in front of the vacuum chamber.

has a longer distance to cover passing the chamber windows, so less light should be transmitted. Although this effect seems to play a role, it has a rather small impact on the transmission and can be neglected. This can be seen by computing the asymptotic limit for the beam radius evolution where the beam divergence is maximal. The beam radius $w(z)$ can then be approximately described by

$$w(z) = w_0\sqrt{1 + (\frac{z}{z_0})^2} \rightarrow w(z) = \frac{w_0}{z_0}z = \frac{\lambda}{\pi w_0}z\,. \tag{5.18}$$

The angle $\phi$ between a perpendicular chamber window transmission direction and the transmission direction actually taken can then be calculated to fulfil the relation

$$\phi = arctan(\frac{\lambda}{\pi w_0})\,. \tag{5.19}$$

For a wavelength $\lambda = 780nm$ and a beam waist of $w_0 = 40nm$, $\phi \approx 6 \cdot 10^{-3}$ is calculated. Thus, the angle is very small and it can be assumed that the laser beam does transmit the chamber windows in perpendicular direction.
The coupling efficiencies shown in table 5.2 have not been found to be similar for all of the fibers but distinguish rather drastically from each other. For the sol-gel fiber which has the lowest coupling efficiency, no good Gaussian shaped transversal intensity profile could be obtained. This explains why the coupling efficiency value measured is that low. For the other fibers, however, the transversal beam profile has been observed to coincide well with the Gaussian mode. The hollow core fiber analysed in 3.3 had a coupling efficiency of roughly $65 - 75$ per cent for the $50mm$ and $100mm$ lens. Only the efficiency of the PDMS H8003 fiber is located within this vicinity. The PDMS H2006 fiber has a transmission close to 100 per cent. This result reveals that it should in principle also be possible to obtain such a good transmission for other fibers as well. Omitting the result obtained for the sol-gel coated H2006 fiber, the PDMS H3307 and PDMS I1407 have a loss of about 50 per cent. This raises the question

where the rest of the light has gone. For the hollow core fiber outside the vacuum chamber, the lens could easily be replaced and the focussed beam could be observed up to the fiber tip. The adjustment of the lens in front of the vacuum chamber was more difficult and therefore the precision in lens placement was not as good. Thus, the beam radius at a fiber tip for a fiber inside the vacuum chamber could have deviated from the waist radius by more than for the fiber outside the chamber and led to a lower coupling efficiency by scattering processes. The hollow core fiber outside the chamber has a much smaller radius than the other fibers inside the chamber. Since a large contribution of the beam power for this fiber fell onto the cladding structure, it could very well be that light has been scattered away at the tip which resulted in a power loss of $25 - 35$ per cent. Similarly, also light scattering on the fiber tips for the fiber placed inside the vacuum chamber could have led to a drastic reduction in beam transmission.

# 6. Conclusions and future work

In the experiments carried out throughout this thesis, a small vacuum system filled with Kagome hollow core photonic crystal fibers has been analysed. This setup forms part of the project "strong interactions inside hollow core fibers". It is used to find an appropriate fiber for investigating photon-photon interactions inside a confined structure where the interaction probability between photons is enhanced. Within this thesis, a focus has been put on investigations of the vacuum system itself, the laser beam properties and its guidance through fibers.
Therefore, the characteristics of the laser mode has been investigated together with the coupling of light into spatially confined structures provided by the different hollow core fibers. Moreover, the diffusion dynamics for rubidium filling the hollow core fibers has been analysed, since a completed filling process is a prerequisite for performing light-matter interactions within the fibers and it was unknown, how much time the fiber filling required. Finally, the steady state rubidium pressures inside a pyrex glass cell, the vacuum chamber and five different hollow core fibers have been determined.
The laser mode has been analysed with respect to its transversal profile and beam radius evolution behind a glass fiber and a hollow core fiber outside the vacuum system. The transversal profile coincided well with a Gaussian distribution behind the glass fiber. It was then tried to optimize the coupling into the fibers trying to get a Gaussian laser mode after the laser light has passed through the fiber. The beam radius evolution could mostly be confirmed by the experiments done. Its analysation also allowed to check the mode field diameter of the hollow core fiber outside the chamber by the beam waist calculation. It turned out that the mode field diameter could be reproduced quite well out of the beam waist calculation. The paraxial approximation of the beam evolution has therefore been observed to still hold for a beam waist that is roughly twenty times larger then the wavelength of the laser light transmitting the fiber. The coupling efficiencies of light transmitting the fibers have yielded a quite intermixed picture. One fiber revealed that the coupling efficiency can indeed be optimized to get close to a transmission of 100 per cent of the light entering the fiber. For the other fibers, the coupling has been worse by far. This result led to the conclusion that the coupling is highly sensitive on the lenses' placement and focussing strength, even though a fiber is transmitted by a mode dominated by a Gaussian intensity distribution.
The calculations regarding the diffusion revealed that the filling times of rubidium atoms migrating into the hollow core fibers are not only strongly dependent on the fiber radius but also on wall interactions for being deep inside the molecular flow regime. It has been problematic that not all parameters required for calculating the

diffusion process have been known well. Furthermore, it has been missed to record the absorption signals in the time period of significant change where a fit to the calculations could have been done. This restricted the theoretical calculations from being tested experimentally. The results of the calculations have ultimately been taken to give an estimate on the order of magnitude of time the diffusion process really took for the atoms to fill the hollow core fibers. For a silica surface, the fiber filling has been taken to be completed in a time frame of a few days up to two weeks for all of the fibers. For the PDMS and sol-gel coated fibers, the corresponding times scale inversely with the mean absorption time. This quantity unfortunately remained unknown for these coatings. The only information is given by the observation that the PDMS coated fiber with largest radius has been completely filled with rubidium after a few days. In summary, it has been discovered that the surface interaction can be responsible for a variation of filling times over several orders of magnitude. The progress of atoms propagating to the inner fiber domain is dependent on the square of the radius of the fiber. Therefore, reducing the fiber radius by far leads to a remarkable prolongation of the filling process of fibers by atoms. These results explain why the diffusion dymanics can take even month to complete rather than hours or days.
For the pressure calculations of rubidium inside the pyrex glass cell, the vacuum chamber and the five fibers placed inside the vacuum chamber, the rubidium vapour pressure at room temperature has been used as a reference. The rubidium pressure only coincides with the vapour pressure in a pure rubidium environment. Inside the gas hosts available, the conditions are modified by the different kinds of wall material enclosing the rubidium atoms. These measurements have been carried out a few weeks after the rubidium release into the vacuum chamber. According to the diffusion calculations, steady state conditions for the rubidium diffusion inside the whole vacuum system should have been established by then. For the pyrex glass cell, there has been observed a coincidence of calculated pressure and vapour pressure which confirms pyrex glass to be a good choice for hosting rubidium and probably even other alkali metalls. For the vacuum chamber, the calculated pressure has been slightly lower than the vapour pressure. The walls of the chamber are comprised of a metallic and thus non dielectric material. This surface should consequently bind the rubidium atoms stronger than it would be the case of a pure rubidium system. For the five hollow core fibers, the pressures calculated turned out to be one order of magnitude smaller than the vapour pressure. Why the pressure is this much less inside the fibers is not known. There does furthermore not seem to be a clear ordering with respect to fiber radius or wall material. Such a systematic classification has not been possible, as only five fibers out of 18 have been investigated in this regard.

In the frame of this thesis, the goal of choosing an appropriate fiber for the main project has not been achieved, since the focus has mainly been put on investigations of the vacuum system itself, the laser beam properties and its guidance through fibers.
The further work with the system would consist of a detailed characterisation of all

of the fibers inside the vacuum chamber. This would include the quantification of the coupling efficiencies for laser light passing through the fibers, the effects of the inner fiber walls on neutral atoms and the analysis of atoms excited to Rydberg states.

In dieser Arbeit wurde ein Vakuumsystem untersucht, in das Hohlkernfasern ebenso wie ein Rubidium Reservoir integriert sind. Die Eigenschaften von Laserstrahlung sowie sowohl deren Einkopplung in Fasern als auch deren Wechselwirkung mit dem Rubidium im Inneren der Kammer wurden analysiert.
Die Eigenschaften der Laserstrahlung stimmten gut mit den Vorhersagen der Paraxialnäherung überein. Eine Lösung dieser Näherung ist der Gaußstrahl, dessen vorhergesagte transversale Intensitätsverteilung und Strahlbreitenentwicklung entlang der Ausbreitungsachse in den durchgeführten Experimenten bestätigt werden konnte. Die Lichtleitung durch die Fasern lieferte ein gemischtes Bild. Die Kopplungseffizienzen wichen stark voneinander ab. Die Untersuchungen an einer Faser zeigten jedoch, dass es möglich ist, bis auf wenige Prozent eine vollständige Transmission zu erzielen. Die im Vergleich dazu eher schlechten Effizienzen für die anderen Fasern wurden dadurch erklärt, dass die fehlende Strahlung hinter der jeweiligen Faser am Fasereingang weggestreut worden sein muss.
Bei der theoretischen Behandlung der Diffusion traten mehrere Schwierigkeiten auf. Zum Einen waren nicht alle Diffusionsparameter für die theoretische Behandlung genau bekannt. Zum Anderen fehlte ein guter Vergleich mit dem Experiment, da der Zeitraum wesentlicher Änderungen im aufgenommenen Absorptionssignal von Rubidium in den Fasern, der Aufschluss über das Voranschreiten des Diffusionsprozesses hätte geben können, verpasst wurde. Bei der theoretischen Behandlung wurde festgestellt, dass die Dauer der Atommigration quadratisch mit dem Faserradius zusammenhängt und im Falle des niedrigen Rubidiumdampfdrucks bei Raumtemperatur die Wechselwirkung mit der Faserinnenwand drastischen Einfluss auf diese hat. Für die in der Vakuumkammer integrierten Fasern wurde das Erreichen eines stationären Zustandes in Bezug auf die Diffusion auf wenige Tage bis etwa zwei Wochen geschätzt. Die Erkenntnisse legen nahe, dass das Fortschreiten der Diffusion bei kleineren Fasern mit langen Atomadsorptionszeiten an der Faserwand durchaus auf viele Monate hinaus verzögert werden kann.
Die ermittelten, stationären Rubidiumdrücke in der Pyrexglaszelle, der Vakuumkammer und fünf der achtzehn Fasern in der Vakuumkammer sind mit dem zugehörigen Dampfdruck bei Raumtemperatur verglichen worden. Abweichungen vom Dampfdruck sind auf die Wechselwirkungen mit dem umgebenden Material zurückgeführt worden. Für die Pyrexglaszelle stimmte der ermittelte Druck im Rahmen des Fehlers mit dem Dampfdruck überein, was als Bestätigung dafür gewertet wurde, dass sich Pyrex Glas gut eignet als Gefäßmaterial zur Speicherung von Rubidium(gas). Wahrscheinlich gilt das auch für andere Alkalimetalle. In der Vakuumkammer war der Druck etwas kleiner. Hier handelte es sich um eine metallische Wechselwirkungsoberfläche, die Rubidiumatome gut an sich zu binden scheint. Im Fall der Fasern lag der ermittelte Druck etwa eine Größenordnung unterhalb des Dampfdrucks. Warum

der Druck so niedrig ist, konnte nicht plausibel gemacht werden.

# 7. Acknowledgements

I would like to thank the whole Windpassinger research group for providing a matey atmosphere throughout the time I worked on this Bachelor thesis. I especially thank Prof. Dr. Patrick Windpassinger and above all Maria Langbecker and Mohammad Noaman for giving me helpful feedback and advises during the creation of this thesis.

# A. Appendix

## A.1. Tables and figures

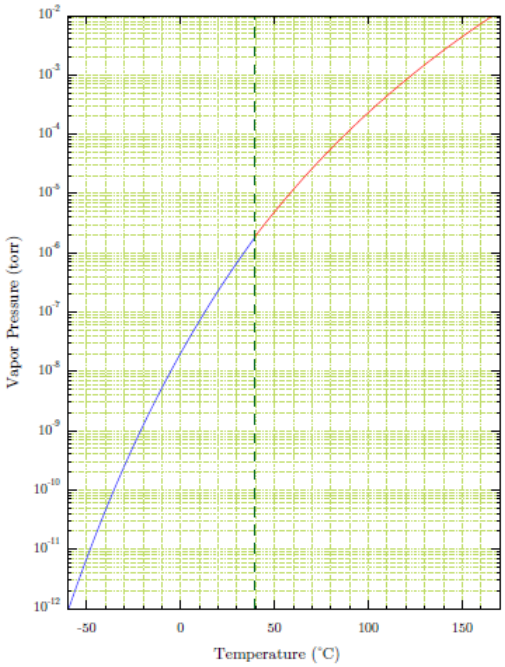


Figure A.1.: Vapour pressure curve for $^{85}Rb$. The dotted line indicates the melting point of the rubidium isotope. The diagram has been taken from [37].

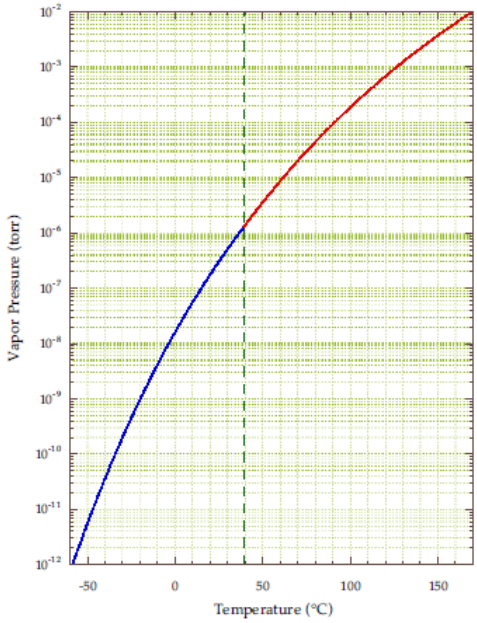


Figure A.2.: Vapour pressure curve for $^{87}Rb$. The dotted line indicates the melting point of the rubidium isotope. The diagram is taken from [38].

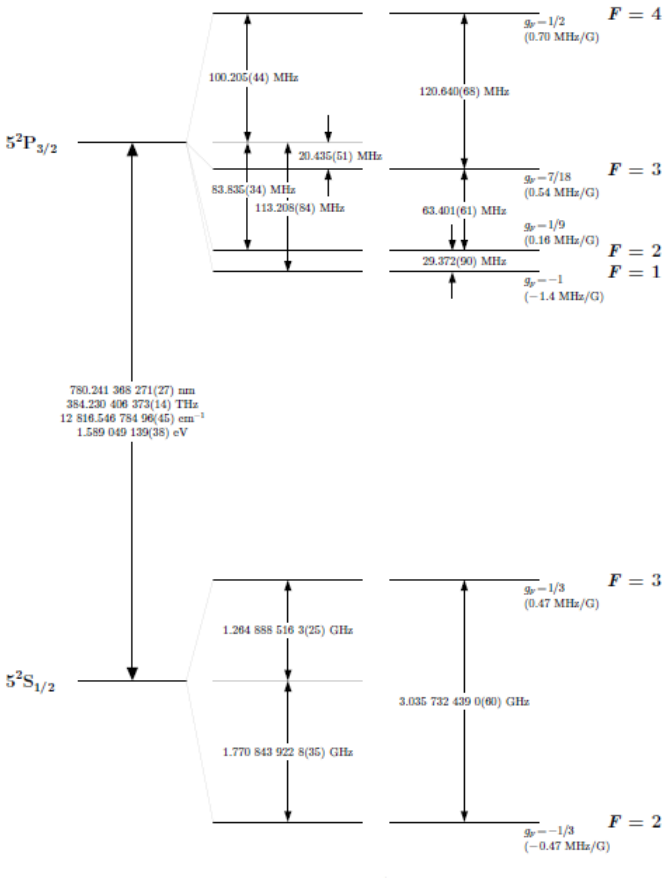


Figure A.3.: $^{85}$Rb transition hyperfine structure, with frequency splittings between the hyperfine energy levels. The approximate Lande $g_F$-factors for each level are also given, with the corresponding Zeeman splittings between adjacent magnetic sublevels. The diagram is taken from [37].

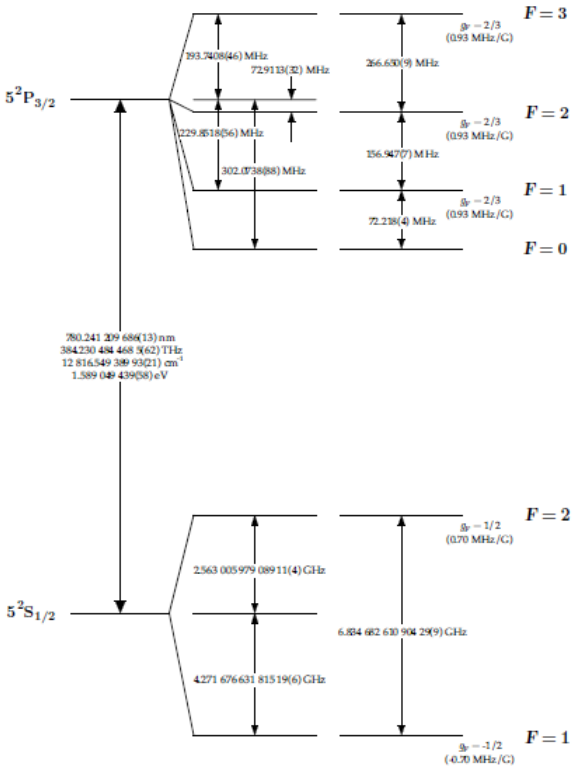


Figure A.4.: $^{87}$Rb transition hyperfine structure, with frequency splittings between the hyperfine energy levels. The approximate Lande $g_F$-factors for each level are also given, with the corresponding Zeeman splittings between adjacent magnetic sublevels. The diagram is taken from [38].

(a)

| $F_g$ | $F_e$ | | | |
|---|---|---|---|---|
| | 1 | 2 | 3 | 4 |
| 2 | $\frac{1}{3}$ | $\frac{35}{81}$ | $\frac{28}{81}$ | 0 |
| 3 | 0 | $\frac{10}{81}$ | $\frac{35}{81}$ | 1 |

(b)

| $F_g$ | $F_e$ | | | |
|---|---|---|---|---|
| | 0 | 1 | 2 | 3 |
| 1 | $\frac{1}{9}$ | $\frac{5}{18}$ | $\frac{5}{18}$ | 0 |
| 2 | 0 | $\frac{1}{18}$ | $\frac{5}{18}$ | $\frac{7}{9}$ |

Figure A.5.: Values of the transition strength factors $C_F^2$ of the $D_2$-lines of $^{85}$Rb (a) and $^{87}$Rb (b). Taken from [36].

# References

## A.2. References

[1] Takamoto M, Hong F-L, Higashi R, Katori H. An optical lattice clock. Nature [Internet]. 2005 May 19 [cited 2013 Feb 1];435(7040):321–4. Available from: http://www.ncbi.nlm.nih.gov/pubmed/15902252

[2] Le Targat R, Lorini L, Le Coq Y, Zawada M, Guéna J, Abgrall M, et al. Experimental realization of an optical second with strontium lattice clocks. Nature Communications [Internet]. 2013 Jul 9 [cited 2013 Jul 10];4. Available from: http://www.nature.com/doifinder/10.1038/ncomms3109

[3] Wynands R, Weyers S. Atomic fountain clocks. Metrologia [Internet]. 2005 Jun 7 [cited 2013 Jun 13];42(3):S64–S79. Available from: http://stacks.iop.org/0026-1394/42/i=3/a=S08?key=crossref.73cd3d68326b49d8f212d76e5079625d

[4] Jefferts SR, Shirley J, Parker TE, Heavner TP, Meekhof DM, Nelson C, et al. Accuracy evaluation of NIST-F1. Metrologia [Internet]. 2002 Aug 1;39(4):321–36. Available from: http://stacks.iop.org/0026-1394/39/i=4/a=1?key=crossref.19a7aee8f7486e26152c728d2f73df6e

[5] Lombardi MA, Heavner TP, Jefferts SR. NIST Primary Frequency Standards and the Realization of the SI Second. The Journal of Measurement Science. 2007;2(4).

[6] Corwin KL, Lu ZT, Hand CF, Epstein RJ, Wieman CE. Frequency-stabilized diode laser with the Zeeman shift in an atomic vapor. Applied optics [Internet]. 1998 May 20;37(15):3295–8. Available from: http://www.ncbi.nlm.nih.gov/pubmed/18273286

[7] Mcferran JJ, Magalhães D V, Mandache C, Millo J, Zhang W. 199 Hg 1 S 3 P clock transition with Laser locking to p the. 2012;37(17):3477–9.

[8] Ensher JR, Matthews MR, Wieman CE, Cornell EA. Observation of Bose- Einstein Condensation in a Dilute Atomic Vapor. 1(ii):4–7.

[9] Phillips WD. Laser cooling and trapping of neutral atoms *. Re-

# References

views of Modern Physics. 1998;70(3):721–41.

[10] Grimm R, Ovchinnikov YB. Optical dipole traps for neutral atoms. Advances In Atomic, Molecular and Optical Physicss. 1987;42(2000):95–170.

[11] Sheng D, Li S, Dural N, Romalis M V. Subfemtotesla Scalar Atomic Magnetometry Using Multipass Cells. 2013;160802(April):1–5.

[12] Budker D, Kimball D, Rochester S, Yashchuk V, Zolotorev M. Sensitive magnetometry based on nonlinear magneto-optical rotation. Physical Review A [Internet]. 2000 Sep;62(4):043403. Available from: http://link.aps.org/doi/10.1103/PhysRevA.62.043403

[13] Knappe S, Shah V, Schwindt PDD, Hollberg L, Kitching J, Liew L-A, et al. A microfabricated atomic clock. Applied Physics Letters [Internet]. 2004 [cited 2013 Feb 13];85(9):1460. Available from: http://link.aip.org/link/APPLAB/v85/i9/p1460/s1Agg=doi

[14] James Camparo. The rubidium atomic clock and basic research. Physics today, American institute of physics. November 2007.

[15] Spillane S, Pati G, Salit K, Hall M, Kumar P, Beausoleil R, et al. Observation of Nonlinear Optical Interactions of Ultralow Levels of Light in a Tapered Optical Nanofiber Embedded in a Hot Rubidium Vapor. Physical Review Letters [Internet]. 2008 Jun [cited 2013 Feb 13];100(23):233602. Available from: http://link.aps.org/doi/10.1103/PhysRevLett.100.233602

[16] Yang W, Conkey DB, Wu B, Yin D, Hawkins AR, Schmidt H. Atomic spectroscopy on a chip. Nature Photonics [Internet]. 2007 Jun [cited 2013 Feb 13];1(6):331–5. Available from: http://www.nature.com/doifinder/10.1038/nphoton.2007.74

[17] Ghosh S, Bhagwat A, Renshaw C, Goh S, Gaeta A, Kirby B. Low-Light-Level Optical Interactions with Rubidium Vapor in a Photonic Band-Gap Fiber. Physical Review Letters [Internet]. 2006 Jul [cited 2013 Feb 13];97(2):023603. Available from: http://link.aps.org/doi/10.1103/PhysRevLett.97.023603

[18] Light PS, Benabid F, Couny F, Maric M, Luiten a N. Electromagnetically induced transparency in Rb-filled coated hollow-core photonic crystal fiber. Optics letters [Internet]. 2007 May 15;32(10):1323–5. Available from: http://www.ncbi.nlm.nih.gov/pubmed/17440575

[19] Thomas David Bradley. Atomic vapours filled hollow core photonic

# References

crystal fibre for magneto-optical spectroscopy. University of Bath, Department of Physics, September 2013.

[20] Dr. Benoit Debord. Research group XLIM, Limoges.

[21] Dietrich Marcuse. Light transmission optics. Second edition. 1972.

[22] Christian Veit. Rf Dressing of Rydberg States in Hollow-Core Fibers. Master thesis. Stuttgart, March 2015.

[23] G.Epple, K.S.Kleinbach, T.G.Euser, N.Y.Joly, T.Pfau, P.St.J.Russell, R.Löw. Rydberg atoms in hollow-core photonic crystal fibers. Nature communications. June 2014.

[24] Isabelle Dicaire, Jean-Charles Beugnot, Luc Thevenaz. Analytical modeling of the gas-filling dynamics in photonic crystal fibers. Applied optics/Vol 49, No.24. August 2010

[25] Wolfgang Demtröder. Experimentalphysik 1: Mechanik und Wärme, 6. edition

[26] J.C.Slater. Atomic radii in crystals. J.Chem.Phys. 1964. 39, 3199.

[27] P. Clausing. Uber die Adsorptionszeit und ihre Messung durch Stromungsversuche. Annalen der Physik, 7(4):489520, NOV 1930.

[28] P.Clausing. On the molecular flow with Langmuirian adsorption of the molecules on the wall of the tube; a correction. Physica 28, page 298-302. 1962

[29] H.N.de Freitas, M.Oria, M.Chevrollier. Spectroscopy of cesium atoms adsorbing and desorbing at a dielectric surface. Appl. Phys. B 75, 703–709 (2002)

[30] J.A.Sedlacek, E.Kim, S.T.Rittenhouse, P.F.Weck, H.R.Sadeghpour, J.P.Shaffer. Electric field cancellation on quartz: a Rb adsorbate induced negative electron affinity surface. arXiv. November 2015

[31] David R. Scherer, David B. Fenner, and Joel M. Hensley. Characterization of Alkali Metal Dispensers and Non-Evaporable Getter Pumps in Ultra-High Vacuum Systems for Cold Atomic Sensors. arXiv. 2012. page 6

[32] L.C.Evans. Partial Differential equations. American Mathematical Society. 1998.

# References

[33] Saikat Ghosh, Amar R. Bhagwat, C. Kyle Renshaw, Shireen Goh, and Alexander L. Gaeta. Low-Light-Level Optical Interactions with Rubidium Vapor in a Photonic Band-Gap Fiber. Physical review letters. July 2006.

[34] Wei Chen, Xinbing Wang, Lian Duan, Quanzheng Xu. The study of hollow fiber gas-filling. OSA. 2012.

[35] Isabelle Dicaire, Jean-Charles Beugnot, Luc Thévenaz. Analytical modeling of the gas-filling dynamics in photonic crystal fibers. Applied Optics / Vol. 49, No. 24. August 2010.

[36] Paul Siddons, Charles S. Adams, Chang Ge, Ifan G. Hughes. Absolute absorption on the rubidium D lines: comparison between theory and experiment. arXiv. 2008

[37] Daniel A. Steck. Rubidium 85 D line data. September 2013. available from: http://steck.us/alkalidata

[38] Daniel A. Steck. Rubidium 87 D line data. October 2003. available from: http://steck.us/alkalidata